Effects of liquid viscosity and bubble size distribution on bubble plume hydrodynamics

David Laupsien, Claude Le Men, Arnaud Cockx, Alain Liné

CHERD-4633; No. of Pages 19

Chemical Engineering Research and Design xxx (2021) xxx–xxx

Contents lists available at ScienceDirect

Chemical Engineering Research and Design

journal homepage: www.elsevier.com/locate/cherd

Effects of liquid viscosity and bubble size distribution on bubble plume hydrodynamics☆

David Laupsien, Claude Le Men, Arnaud Cockx, Alain Liné*

TBI, University of Toulouse, CNRS, INRA, INSA, Toulouse, France

ARTICLE INFO

Article history:
Received 31 March 2021
Received in revised form 9 September 2021
Accepted 22 September 2021
Available online xxx

Keywords:
Bubble plume
Viscosity effects
Bubble size distribution
Phase averaging

ABSTRACT

The present paper provides a complete databank of bubble plume hydrodynamics in various media characterized by different viscosities in the range 1–100 *mPa.s*. Thus, the influence of the viscosity on bubble plume oscillations and on both liquid and gas velocity fields is studied. The role of the bubble size distribution at different viscosities was also analysed by using two different spargers: a membrane to create ellipsoidal millimetrice bubbles and a slugflow tube to create spherical cap bubbles. Mean velocity profiles, averaged over a large number of plume oscillation periods and corresponding root mean square profiles are discussed, in both phases. Furthermore, void fraction profiles, plume oscillation periods, and bubble size distributions are given for all experimental conditions. Finally, probability density functions and phase averaged profiles in the liquid phase provide additional information. The dependence of bubble plume hydrodynamics on liquid viscosity is huge. At large viscosity, the oscillating plume is damped, regardless of the sparger. Concerning the membrane sparger the viscosity increase modifies the plume oscillation period and its lateral plume expansion, whereas, in the case of the slugflow sparger, only the plume expansion is impacted. Liquid phase hyrdodynamics are weakly affected by the choice of sparger, especially at high viscosities.

1. Introduction

Numerous applications in chemical engineering employ gas injection in large volumes of liquid for purposes of mixing or contact (between phases). In general, simple devices like bubble columns or aeration tanks are used. The former have been extensively studied for decades and multiple investigations can be found in the literature. In the case of bubble columns where the gas injection is homogeneously distributed over the whole column section, the flow regime is generally characterized by the void fraction versus the superficial gas velocity (Hikita et al., 1980; Zahradnik et al., 1997; Ruzicka et al., 2001b). In this way, two main flow regimes can be categorized: the homogeneous (flat horizontal velocity (Lapin and Lubbert, 1994) and void fraction profiles (Kumar et al., 1997) and the heterogeneous regime (non-stationary liquid circulations on short time scales (Chen et al., 1994; Devanathan et al., 1995), plus a transition regime between them. This transition was studied by Leon-Becerril and Line (2001) who predicted bubble flow stability analytically, based on the two-fluid model. They showed destabilizing effects of both bubble deformation and added mass force. Lucas et al. (2005) explained the regime transition via a stability criterion of the lift force. The authors found that a negative lift coefficient (large bubbles) led to a heterogeneous regime, while a positive lift coefficient (small bubbles) stabilized the flow. Recently, Lucas and Ziegenhein (2019) validated this theory in a rectangular bubble column with homogeneous gas injection. They further explained that the criterion is only valid at local scales. However, it should be stated that local instabilities can lead to global instabilities and thus to a heterogeneous flow regime.

☆ Fully documented templates are available in the elsarticle package on CTAN.

* Corresponding author.
E-mail address: laupsien@insa-toulouse.fr (D. Laupsien).

https://doi.org/10.1016/j.cherd.2021.09.025
0263-8762/

A large number of papers have investigated bubble columns with a homogeneous spread concerning column dimensions (Wilkinson et al., 1992; Ruzicka et al., 2001a) and sparger design (Vial et al., 2001; Kazakis et al., 2007; Garmroodi Asil et al., 2020), to name but a few. Other authors have taken an interest in the impact of fluid properties on bubble column hydrodynamics since industrial applications are generally confronted with complex fluids. For example, the impact of viscosity on the flow regime in a cylindrical bubble column with an inner diameter of $0.14\,m$ was investigated by Ruzicka et al. (2003). The authors observed a stabilizing effect of the viscosity on the bubbly flow in the $1-3\,mPa.s$ range. In contrast, viscosity increases in the $3-22\,mPa.s$ range led to coalescence and thus to heterogeneities. A similar study was conducted by Besagni et al. (2017), who were interested in the effect of viscosity on gas holdup, flow regime transition, and bubble size distribution (BSD) in a bubble column with an inner diameter of $0.24\,m$. They observed that coalescence increased with increasing viscosity, modifying bubble sizes and shapes. Resulting large spherical cap bubbles tended to rise in the column centre (negative lift coefficient), thus leading to a heterogeneous flow regime. The same authors studied the influence of surfactants on bubble column hydrodynamics. Ruzicka et al. (2008) chose the salt $CaCl_2$ as surface active agent and reported a dual effect - on the gas holdup and the flow regime stability. The increased surface tension generated smaller bubbles, which stabilized the homogeneous flow regime. Besagni and Inzoli (2017) used different concentrations of $NaCl$ to understand the influence of electrolyte concentration in counter-current flows. They also reported BSDs shifted towards smaller bubbles and a stabilizing effect of surfactants up to a certain critical concentration. These authors concluded that the transition to the heterogeneous flow regime depends on the appearance of coalescence and thus on interface properties, which determine the BSD. Olivieri et al. (2013) investigated the combined effect of surface tension and viscosity on bubble column hydrodynamics. They also concluded that liquid properties strongly impact the transition velocities between flow regimes. The effect on bubble coalescence of surface active additives in viscous solutions and, hence, the flow regime was studied by Zahradnik et al. (1999). In their work, different alcohols were added to aqueous solutions of saccharose in the viscosity range of $1.4-120\,mPa.s$. It turned out that even small amounts of aliphatic alcohol decreased coalescence and stabilized the flow regime. Every alcohol showed the ability to suppress coalescence completely above a transition concentration that depended on the number of carbon atoms in the alcohol molecule. Especially at high viscosities ($\mu_L \geq 8\ mPa.s$), where coalescence was frequent and the flow strongly heterogeneous, the addition of alcohol restored the existence of a homogeneous bubbling regime at intermediate superficial gas velocities ($u_H \leq 0.04\ m/s$). Passos et al. (2015) observed the same stabilizing effect of surfactant addition on bubble column hydrodynamics. BSDs were shifted towards smaller bubbles and transition velocities increased.

As illustrated above, a large number of investigations dealing with cylindrical bubble columns with homogeneous gas injection can be found in the literature. However, in large tanks that are wide compared to their height, the flow regime is more often heterogeneous and the gas injection can also be considered as heterogeneous. Such spargers can then be understood as spot injection devices, leading to the creation of oscillating bubble plumes, which may contribute to mixing and should therefore be studied. Unfortunately, contributions dedicated to bubble plume hydrodynamics in large-scale reactors are rare in the literature. One exception is the work of Simiano et al. (2006), who investigated bubble plumes experimentally in a $2\,m$ diameter vessel with a height of $3.4\,m$, giving void fraction profiles, BSDs, gas and liquid velocities for a large range of gas injection flow rates ($7.5-60\,NL/\,\mathrm{min}$). One important finding was that the average gas spreading was mainly due to the meandering behaviour of the bubble plume. Such information can be useful to understand pneumatic mixing and to optimize sparger locations in large-scale reactors. Some years before, bubble plume oscillations were already investigated in three-dimensional conditions Rensen and Roig (2001) but in a smaller, square bubble column ($150\times150\,mm^2$). The authors used an optical fibre probe and high speed cameras to follow the movement of the geometrical centre of the plume in order to estimate its oscillation frequency. Their non-dimensional analysis enabled comparison with plume oscillation periods (POPs) from other experimental facilities, even with pseudo two-dimensional ones. They concluded that large-scale bubble plume oscillations in confined conditions are mainly buoyancy driven. Since two- and three-dimensional meandering bubble plumes are controlled by similar fluid mechanisms, and, due to the difficulties of investigating the hydrodynamics in large reactors experimentally, researchers studied pseudo two-dimensional bubble columns with spot gas injection instead. In this way, models implemented in numerical simulations can be confronted with precise experimental data because the set-up provides the possibility of applying visual metrological methods like particle-image velocimetry (PIV) or the shadowgraph technique.

Noticeably fewer papers have been published on this subject, especially when it comes to the impact of fluid properties. However, the oscillating bubble plume behaviour in pseudo two-dimensional bubble columns induced by gas injection in quiescent water was first investigated by Becker et al. (1994) and Delnoij et al. (1997) who compared numerical results with experimental data. Delnoij et al. (1997) focused on aspect ratios (height-to-width ratios) ranging from 1 to 11.4 and concluded that bubble plume oscillations take place in the range between 2 and 7.7. Later, further studies were published, focusing on the aspect ratio (Becker et al., 1999; Pfleger et al., 1999; Buwa and Ranade, 2004; Diaz et al., 2006), on sparger design (Lin et al., 1996; Buwa and Ranade, 2004) and on mixing (Buwa and Ranade, 2003). Delnoij et al. (2000) analysed the transient bubble plume behavior in more detail and revealed large-scale structures in flat bubble columns with gas and liquid velocity measurements. Recently, an overview of the key parameters concerning bubble plumes in pseudo two-dimensional conditions was given in Liu et al. (2019). The authors proposed a correlation based on the superficial gas velocity, j_g, the column width, W, and the gravitational acceleration, g, to calculate the oscillation frequency. Unfortunately, fluid properties were not included in their expression and regime transitions not predicted.

As mentioned above, only very few works deal with the impact of fluid properties on bubble plume oscillations. One of them is the paper by Cachaza et al. (2011), investigating the influence of surface tension. After adding surfactants, the authors observed modified BSDs, and at high superficial velocities, regime transitions from an oscillating bubble plume or vortical flow to a double-cell turbulent flow regime (Diaz et al., 2006). Here again, the results suggest a correlation between BSD and flow regime. A previous work (Laupsien et al., 2017)

showed the influence of the viscosity on the POP with two different spargers. It turned out that bubble plume oscillations induced by a membrane sparger are sensitive to the viscosity, unlike those from a slugflow sparger. In the slugflow case, where spherical cap bubbles were injected, the POP remained constant with increasing viscosity. Bubble plumes made up of ellipsoidal bubbles (membrane sparger) and without coalescence show decreasing POPs with increasing viscosity. Once clusters are formed or coalescence appears (at $\geq 50\,mPa.s$) the POP slightly increased again. These examples also indicate a correlation between BSD and bubble plume oscillations. Independently of the bubble column diffuser (homogeneous or heterogeneous sparger design), fluid properties like viscosity and surface tension show great impact on the BSDs. Only in the case of oscillating bubble plumes, does the appearance of coalescence not automatically lead to regime transition. Indeed, POPs are related to the bubble rise velocity and hence to the BSDs, but the plume continues to oscillate even if coalescence appears.

In the present paper, we give a detailed hydrodynamic analysis of bubble plumes. First the gas phase is studied via an optical fibre probe and the shadowgraph technique. POPs, BSDs, void fraction and gas velocity profiles with corresponding root mean square (RMS) in two directions are given for each case considered. The liquid phase was investigated by performing PIV. Local velocity signals with corresponding probability density functions (PDFs) are given first. Then time averaged velocity profiles with corresponding RMS and stress tensor are shown for both spargers and all the fluids considered. All experimental conditions are illustrated by shadowgraph images, and phase (or conditional) average velocity profiles give additional information. The aim of this work is to highlight the periodic structure of hydrodynamics induced by an oscillating bubble plume and to provide a complete data bank to improve oscillating bubble plume modelling.

2. Experimental set-up

2.1. Experimental facility

Experiments were performed in a pseudo two-dimensional bubble column, which was $0.06\,m$ deep, $0.35\,m$ wide and $2\,m$ high. By setting the liquid height to $1.3\,m$, corresponding to a height to width ratio (H/W) of 3.7, regime transitions due to the aspect ratio could be avoided (Diaz et al., 2006). Gas was injected in the centre of the bottom plate with two different spargers, an elastic membrane with an inner diameter of $20\,mm$ to induce ellipsoidal bubbles (EBs) and a slugflow tube (polyvinyl chloride tube) with an inner diameter of $16\,mm$ to induce spherical cap bubbles (CBs), both creating a bubble plume. The gas flow rate was set to $50\,l/h$ corresponding to a superficial gas velocity of $0.66\,mm/s$. Fig. 1 shows the experimental set-up with a dotted rectangle, indicating the PIV and shadowgraph interrogation window. In the following, the column center is referred to $X = 0$ and its wall to $X = 1$ with $X = 2x/W$ and W corresponding to the column width, whereas the vertical axis is Y.

The column is transparent, allowing the use of visual metrological methods. Two CCD cameras (Flowsense from Dantec Dynamics) with $105\,mm$ Nikon Lenses are focused, by means of a beam separator, on the same interrogation window as illustrated in Fig. 1, which is $167\,mm$ wide and $87\,mm$ high,

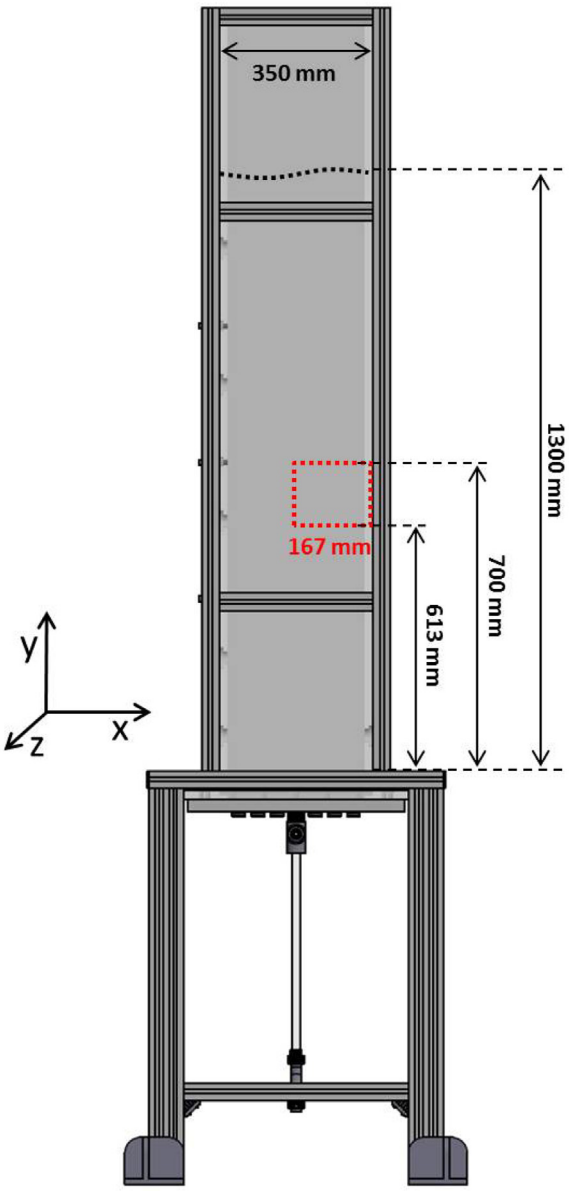

Fig. 1 – Experimental setup: bubble column - front view with the acquisition window indicated as dotted rectangle.

corresponding to 1600 pixels by 840 pixels. It is located at a vertical position (613 to $700\,mm$), where the plume is completely developed as shown in Fig. 2. Covering the right half column is sufficient for the analysis since time averaged data give symmetrical results over the whole column section as long as an integral number of periods is considered. However, the two cameras were perfectly synchronized and the two phases could be separated by using different wavelengths. The acquisition frequency of the cameras was set to $15\,Hz$ with a time interval between image pairs of $2\,ms$.

2.2. Particle-image velocimetry

The first camera was dedicated to the liquid-phase flow field deduced from PIV. Seeding particles ($1 - 20\,\mu m$) from Dantec were covered with Rhodamine B fluorescent dye and showed a maximum light absorption at $532\,nm$ and maximum emission around $590\,nm$. A laser light in the green range ($537\,nm$) was used and a high pass light filter ($> 570\,nm$) was added to the camera. Thus, the camera focused only on the liquid phase and light distrubances could be avoided as far as possible. The

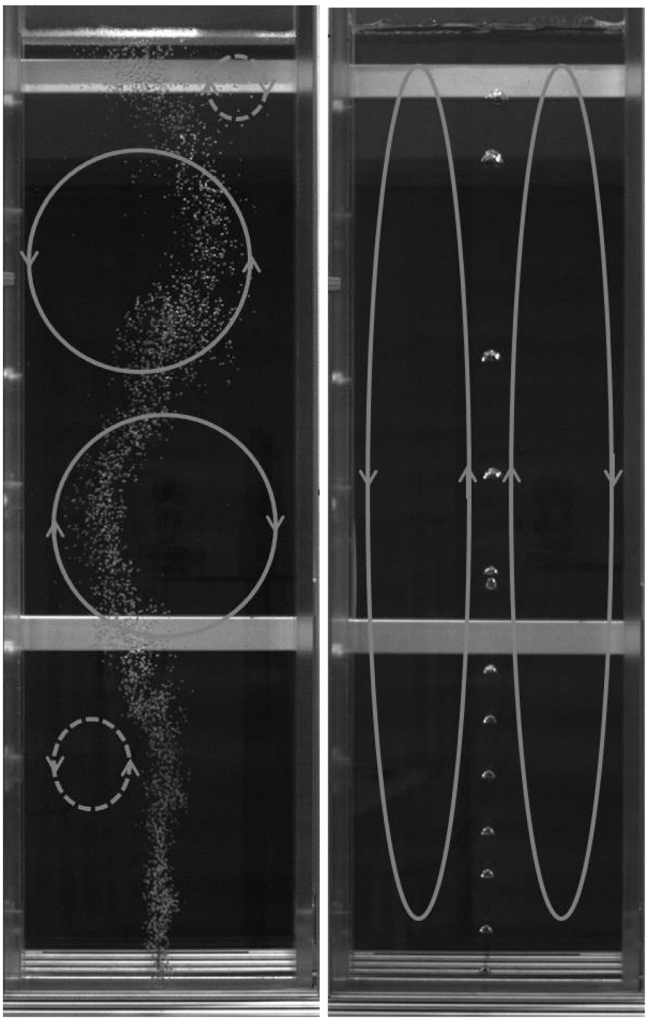

(a) (b)

Fig. 2 – Illustration of flow regimes with membrane sparger (EB) a) water: vortical flow b) fluid B5: double-cell flow.

aperture of the lense was set to its maximum to reduce the depth of the field of view. The laser light intensity was adapted to capture a sufficient amount of light all by avoiding satured pixels on the greylevel histogram. However, an adaptive PIV method included in DynamicStudio from Dantec gives 16 × 16 pixel cross-correlation matrices, corresponding to 99 vectors in length and 51 in height. The vector resolution obtained is 1.67 *mm*. Furthermore, a conditional median filter included in DynamicStudio enables the correction of false vectors due to light disturbances on gas-liquid interfaces. For further details we refer the reader to a preliminary study published in a previous paper (Laupsien et al., 2021a).

2.3. *Shadowgraph technique*

The second camera was also used in double frame mode, as for PIV, and provided shadowgraph image pairs to study gas velocities, BSD and void fraction profiles (Laupsien, 2017). To focus only on the gas phase a blue LED panel (CCS-LFL-200BL2) with a peak wavelength around 470 *nm* and a low pass filter (< 500 *nm*) were used. The velocity of each individual object could be obtained from shadowgraph images via Labelled Object Velocimetry (LOV) developed by Laupsien et al. (2021b). Algorithm-based object selection (Laupsien et al., 2019) was applied to the first frame of image pairs in order to investigate the bubble morphology and BSD. In this study, the shadowgraph technique was integrated over the whole column depth, due to the great depth of the field of view, which implies a large aperture of the lense. The light intensity of the LED panel was then adapted to capture a sufficient amount of light all by avoiding satured pixels on the grey level histogram, as for the PIV camera. The LED panel was connected to a voltage drive with pulse width modulation from Gardasoft to attain 500% of the maximum light intensity with a constant-current drive source. However, to analyse the gas velocity correctly, the object size must be taken into account, especially if the BSD is wide. For gas velocity averaging, every object has to be weighted, which can be done either via the volume or via the projected two-dimensional area. Here, the latter was chosen to avoid volume reconstructions of complex objects such as coalescing, breaking or overlaying bubbles. The gas velocity weighting can be described by the following equation:

$$\bar{U_g} = \frac{\sum_{i=1}^{N} A_{raw_i} U_{g_i}}{\sum_{i=1}^{N} A_{raw_i}} \tag{1}$$

where A_{raw_i} corresponds to the raw projected object area and U_{g_i} to its velocity. $\bar{U_g}$ gives the final swarm velocity for each spatial interval along the horizontal axis (Laupsien et al., 2021b). The corresponding weighted RMS can be expressed as:

$$U_{g,RMS} = \sqrt{\frac{\sum_{i=1}^{N} A_{raw_i} (U_{g_i} - \bar{U_g})^2}{(N-1)\sum_{i=1}^{N} A_{raw_i}}} \tag{2}$$

2.4. *Optical probe*

To complete void fraction data, complementary measurements were performed with an optical probe from A2 Photonic Sensors. At a height of 650 *mm*, local long-time void fraction measurements of at least 20 minutes, depending on the position, were recorded at an acquisition frequency of 100 *kHz*. The optical probe was moved by 5 *mm* along the *X*-axis between two consecutive measurements.

2.5. *Fluids and flow structure*

To investigate the influence of fluid properties and especially the viscosity, a copolymer called Breox from BASF (CAS Number: 9003-11-6) was used to produce different fluids with Newtonian behaviour. The exact liquid properties are listed in Table 1. Water and fluid B1 have the same viscosity, but different surface tensions whereas fluids B1 to B5 have the same surface tension, but different viscosities.

Depending on fluid properties, two flow regimes could be identified during this study. The first one, illustrated in Fig. 2a, corresponds to the Vortical Flow as proposed by (Diaz et al., 2006). The case considered here corresponds to the membrane sparger and water. Bubbles rise on a sinusoidal trajectory, known as the typical bubble plume shape. The plume oscillates and generates liquid vortex cells at the free surface on the opposite side to the bubble release. Each vortex remains close to the free surface and grows until it covers nearly the whole column width. Once its maximum size is reached, the vortex begins to descend. At the same time, the vortex close to the bottom dissipates. Thus, two completely developed vortex cells covering the whole column width and descending towards the bottom always exist in the case of the aspect ratio considered. Each vortex that disappears is renewed by a new

Table 1 – Fluid properties.

Fluid	Water	B1	B2	B3	B4	B5
Polymer Concentration (%)	0	0.5	8.7	13.6	18.5	24.0
Surface Tension (mN/m) at 20°	75.1	56.8	56.0	55.6	55.6	55.0
Viscosity ($mPa.s$) at 20°	1	1	10	20	50	100
Density at 20° (kg/m^3)	984.7	985.3	994.3	999.7	1005.3	1011.2

Table 2 – Results for ellipsoidal bubbles (EB), $j_g = 0.66$ mm/s.

Fluid	$D_{E,2}$ (mm)	T (s)	f (Hz)	a (-)
Water	5.0	28.2	0.035	0.42
B1	1.3 / 2.9	25.9	0.039	0.48
B2	1.0 / 2.2 / 3.7	22.6	0.044	0.27
B3	1.9 / 4.0	21.4	0.047	0.27
B4	3.5	22.4	0.045	0.19
B5	2.5 / [15-25]	-	-	0.15

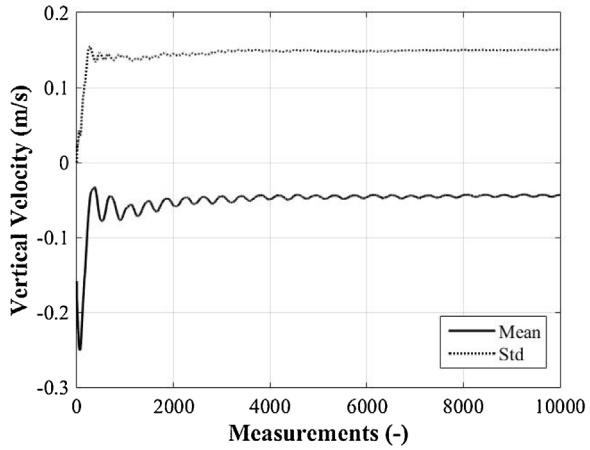

Fig. 3 – Convergence of vertical nean and corresponding RMS liquid velocity in fluid B1 at point X = 0.9.

one at the free surface in a perpetual periodical birth-death cycle.

The second flow regime, illustrated in Fig. 2b, is called Double-Cell Flow (DCF) and inspired by the regime Double-Cell Turbulent Flow as proposed by Diaz et al. (2006). Since fluid B5 is more viscous than water and turbulence is damped, one prefered to remove the term "turbulent". However, bubbles rise along the centreline of the column towards the free surface, generating two symmetrical elongated liquid recirculation cells of the order of the column height. The figure illustrates fluid B5 with bubble injection through the membrane, but the same flow structure was observed in the case of the slugflow sparger. Numerical simulations performed by Etha et al. (2019) for highly viscous fluids confirmed the non-oscillating behaviour.

2.6. *Plume oscillation period and convergence*

The bubble plumes obtained (Fig. 2a) show low frequency oscillations with POPs ranging from ≈ 20 s to ≈ 30 s (Table 2). A sufficiently large number of periods was required to reach statistical convergence as shown in Fig. 3. The figure shows mean and RMS liquid velocities in the case of fluid B1 characterized by a decreased surface tension compared to water. As illustrated in Fig. 3, about 5000 measurement points, corresponding to 13 bubble plume oscillations (1 period is equal to 25.9 s) were necessary to be sufficiently statistically reliable for hydrodynamic data to be averaged.

Table 3 – Results for cap bubbles (CB), $j_g = 0.66$ mm/s.

Fluid	$D_{E,2}$ (mm)	T (s)	f (Hz)	a (-)
Water	5.8 / [15-40]	25.7	0.039	0.29
B1	4.4 / [15-40]	26.5	0.038	0.36
B2	4.2 / [15-35]	25.9	0.039	0.27
B3	4.2 / [5-40]	26.3	0.038	0.23
B4	5.0 / [5-35]	-	-	0.16
B5	4.4 / [5-30]	-	-	0.09

3. Results and discussion: gas phase

In this section, the gas phase of the bubble plume is studied in detail. Overall results, concerning the membrane and the slugflow sparger are summarized in Tables 2 and 3 , respectively. Median bubble sizes ($D_{E,2}$), POPs (T), corresponding oscillation frequencies (f) and plume expansions (a) defined as the plume width at 50% of the normalized void fraction (Figs. 8a and b) and normalized by the column width, are given for all flow conditions.

In subsection 3.1 the POP is used to characterize the hydrodynamic bubble plume behaviour. Then, BSDs (subsection 3.2) and void fraction profiles (subsection 3.3) are presented for all experimental conditions. Finally, time averaged horizontal profiles of the gas velocity and corresponding root mean square (RMS) are analysed in subsection 3.4.

3.1. *Plume oscillations*

In the experimental conditions considered, bubble plumes show oscillating behaviour, which depends on the superficial gas velocity (Buwa and Ranade, 2004; Diaz et al., 2006; Laupsien et al., 2017), the aspect ratio of the bubble column (Diaz et al., 2006), sparger design (Buwa and Ranade, 2004; Laupsien et al., 2017), surface tension (Cachaza et al., 2011; Laupsien et al., 2017) and viscosity (Laupsien et al., 2017). The influence of the last three and especially of the viscosity, is within the scope of the present paper. To characterize the oscillating behaviour, the POP or its frequency can be useful. Both are given in Table 2 for the membrane sparger and in Table 3 for the slugflow sparger.

In the case of ellipsoidal bubbles created by the membrane sparger, increasing viscosity decreases the POP. Once clustering (fluid B4) or coalescence (fluid B5) appears the POP increases again, slightly. At the highest viscosity (fluid B5), no plume oscillations could be observed. Furthermore, the POP is also affected by the decreased surface tension (fluid B1). In the case of large bubbles created by the slugflow sparger, viscosity as well as surface tension modifications have practically no impact on the POP, which is constant (≈ 26 seconds) for the experimental conditions considered. At a viscosity of 50 $mPa.s$ (fluid B4) no plume oscillations could be observed with the slugflow sparger.

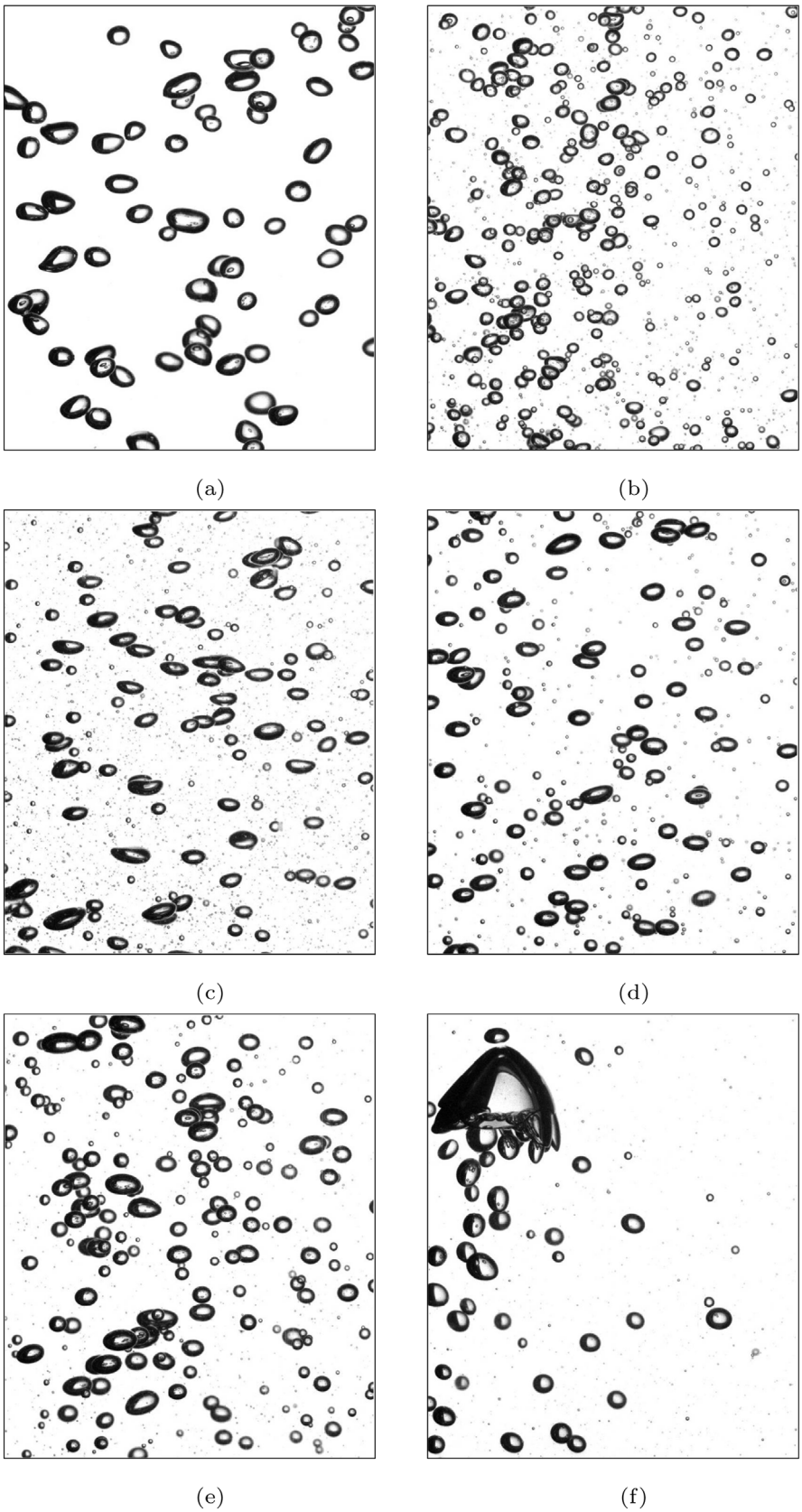

Fig. 4 – Zoom (70 × 84 mm^2) of shadowgraph images with membrane sparger in different fluids: a) water b) B1 c) B2 d) B3 e) B4 f) B5.

Hence, it can be concluded that surface tension, sparger design and viscosity influence the oscillating behaviour, in our case by up to 25% (water compared to fluid B4). In correlations from the literature, these aspects are generally not taken into account. For example, the authors of the latest paper on the subject (Liu et al. (2019)) proposed a correlation, considering exclusively superficial gas velocity, column width and the gravitational acceleration to predict the POP. Their proposition shows good agreement with most data from the literature in water, but in our case it would give a constant frequency

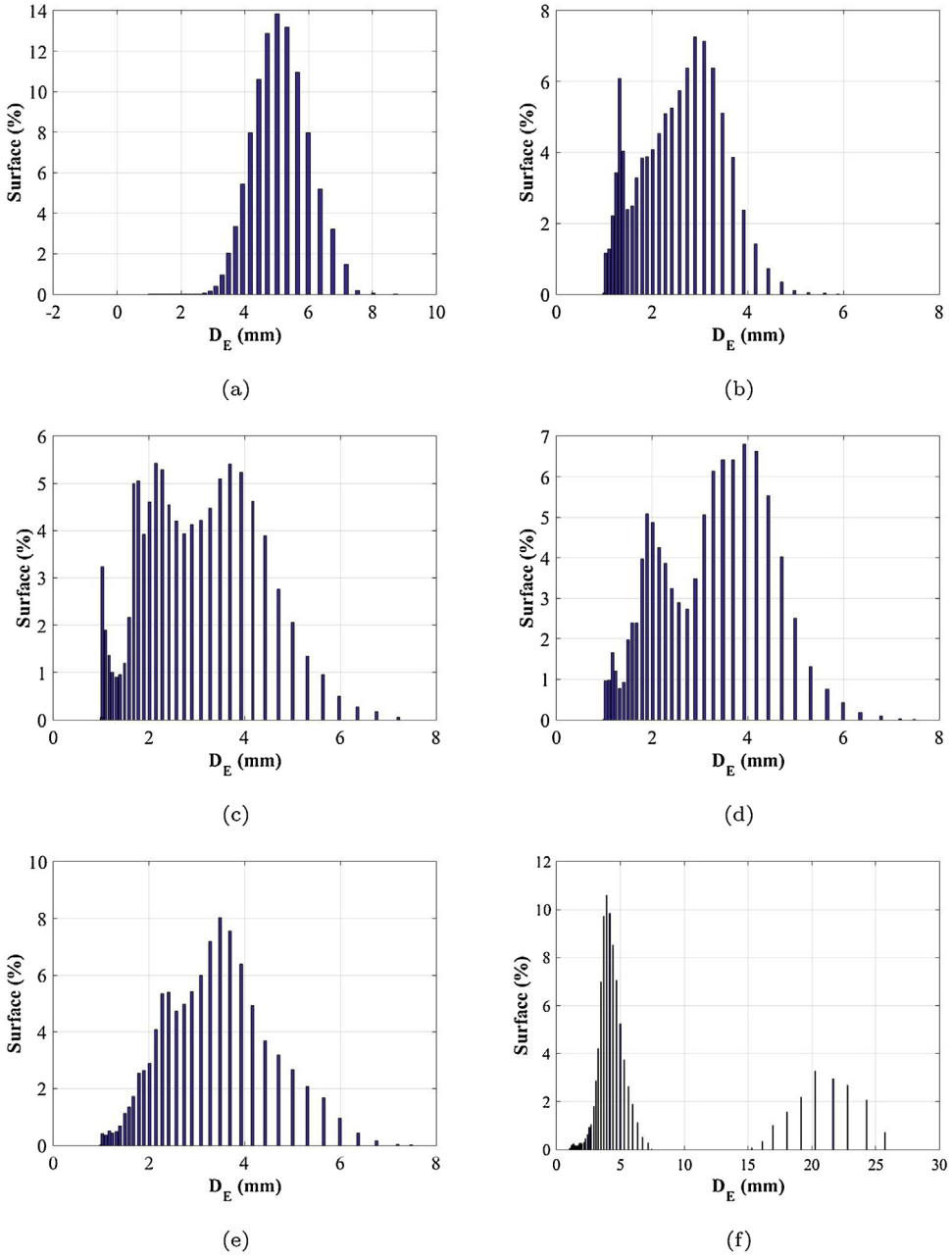

Fig. 5 – BSD with membrane sparger in different fluids: a) water b) B1 c) B2 d) B3 e) B4 f) B5.

of 0.034 *Hz*. To be able to predict the oscillation more precisely, surface tension, sparger design and viscosity should be taken into account. One possibility could be to consider these aspects indirectly via resulting bubble size distributions (BSDs).

3.2. *Bubble size distribution*

BSDs, created by two spargers in different fluids (Section 2), are tackled in this section. As mentioned above and in the literature, they are influenced by sparger design, surface tension and viscosity. Furthermore, the BSD determines rising velocities and bubble interactions, which can lead to modifications of the oscillating plume behaviour.

For the analysis, the algorithm-based object selection developed in (Laupsien et al., 2019) was used to obtain a representative sample of the whole bubble swarm for the experimental conditions considered in this work. It is important to note that the algorithm was applied to a smaller interrogation window, which is why results may differ slightly from those of our previous paper.

However, to illustrate the influence of fluid properties on the BSD, shadowgraph images of each fluid and for both spargers are shown in Figs. 4 and 6 . In the case of the membrane sparger (Fig. 5), an almost monodisperse BSD of EBs is observed in water (Fig. 4a). The corresponding PDF is plotted in Fig. 5a, showing a median bubble size of 5 *mm*. In a fluid with decreased surface tension (fluid B1 - Fig. 4b), the same sparger creates a bimodal BSD as shown in Fig. 5b due to the generation of small bubbles. As expected, the median size of the dominant bubble population decreases to $\approx 3\,mm$. With increasing viscosity (fluid B2 & B3 - Figs. 4c and d), the median bubble sizes shift towards slightly larger values ($\approx 4\,mm$) as plotted in Figs. 5c and d, without the appearance of coalescence or breakups. All bubble populations are generated at the gas injection. Further viscosity increases continue to stablize the bubble interface and generate small clusters as shown in

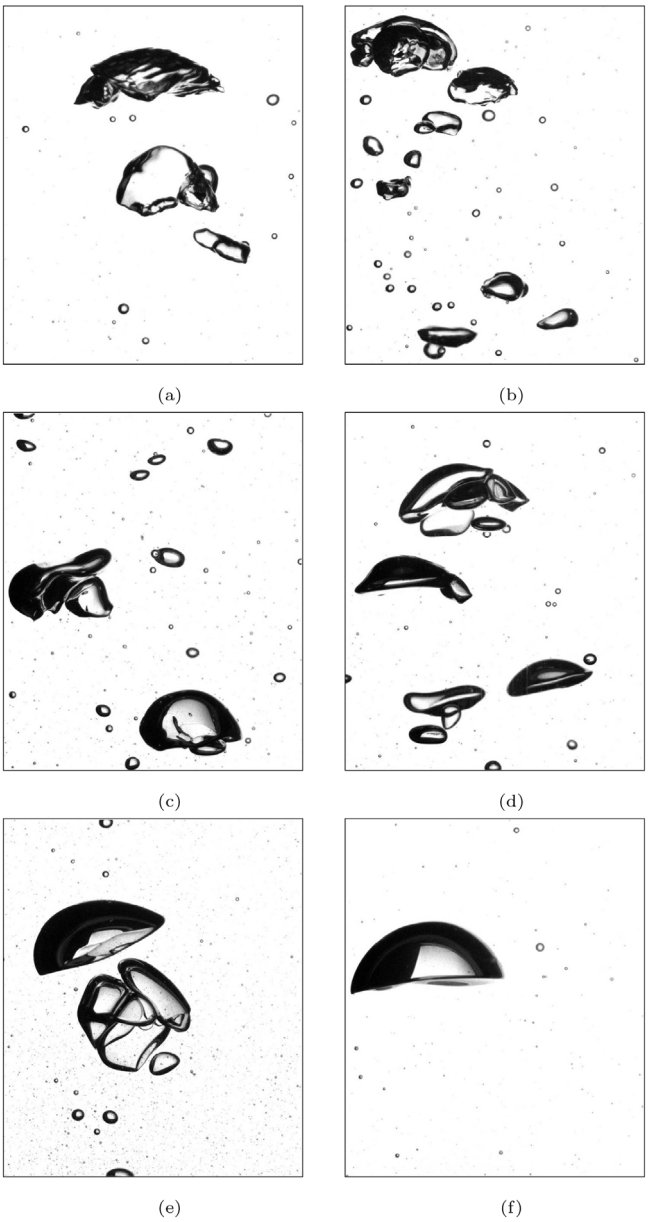

Fig. 6 – Zoom (70 × 84 mm^2) of shadowgraph images with slugflow sparger in different fluids: a) Water b) B1 c) B2 d) B3 e) B4 f) B5.

Fig. 5e. At the highest viscosity considered here, coalescence appears, creating large CBs in addition to EBs (Figs. 4f and 5 f).

A similar analysis was performed in the case of the slugflow sparger (Figs. 6 and 7). First, it must be mentioned that the image treatment of CBs is more diffcult, due to overlays, coalescence and breakups, which renders BSDs very complex. However, median bubble sizes can be recognized for each bubble population. The BSDs are made up of both EBs and CBs, and show a large range of bubble sizes as illustrated in Figs. 6 and 7 .

At low viscosity (water and B1), gas-liquid interfaces are fragile (Figs. 6a and b). The instable behaviour generates all kinds of objects in a large size range and can also be recognized by the instability waves on the bubble interface in Fig. 6a. The increasing viscosity has a stabilizing effect on the interface. At the highest viscosity considered here, mostly very stable CBs, as shown in Fig. 6f, were observed. Without knowing the exact proportions of the different bubble sizes, it can be concluded that large CBs constitute the major proportion of the bubble swarm (Fig. 7f). At intermediate viscosities (fluids B2, B3 and B4), bubble interfaces show round curves at the edges as in water or fluid B1, but with higher stability. Intermediate sized bubbles become more stable and are therefore present in higher numbers than in fluids with very low or high viscosities, where mainly small and/or very large bubbles are present. This becomes particularly obvious in fluids B3 and B4 (Figs. 6d and e) and is confirmed by Figs. 7d and e, where a large number of bubbles with equivalent diameter between 5 *mm* and 15 *mm* can be detected. At low viscosities, objects in this size range are too distorted or interact too much with other bubbles to be identified. Indeed, the ellipse projection used in (Laupsien et al., 2019) works better when stable bubble interfaces with round curves at the edges are studied. With increasing viscosity, round curves become sharp edges until CBs form well shaped half spheres as shown in Fig. 7f. These well shaped CBs were efficiently detected, almost as well as EBs.

3.3. *Void fraction*

The void fraction and its distribution inside the bubble column is important information to characterize the hydrodynamic flow structure. To investigate bubble dispersion, horizontal void fraction profiles were measured by different methods and for all experimental conditions as shown in Fig. 8. It should be mentioned that the width of an oscillating plume is related to the amplitude of its oscillations (Simiano et al., 2006), which is why the plume expansion should be studied in detail, in complement to the POP analysis of Section 3.1

Fig. 8a shows the normalized (by its maximum) projected void fraction profile obtained by the shadowgraph technique in the case of the membrane sparger. The image treatment followed the method presented in Laupsien et al. (2019). After binarization, pixels belonging to the gas phase were summed together in the vertical direction along the horizontal axis. Instantaneous projected void fraction profiles of each image were then averaged over a large integral number of periods, creating the final void fraction profiles shown in Figs. 8a and b. Complementary measurements with an optical probe were performed during this study. Figs. 8c and d show these local void fractions obtained in normalized and dimensional form, respectively. At high viscosities, the optical probe became too intrusive, which is why only fluids with a viscosity up to 20 *mPa.s* (fluid B3) are presented. In the case of the slugflow sparger, no results are shown because CBs tended to avoid the optical probe tip, especially at high viscosities. The shadowgraph technique was the only method capable of providing reliable void fraction profiles. However, Figs. 8a and c show similar results for fluids B1 to B3 and water. The largest plume oscillation amplitude appears at the lowest viscosity considered here (water and fluid B1) and a dual maximum peak is observed around $X \approx 0.2$ if we recall the symmetry of the flow configuration. The slightly larger dispersion in the case of fluid B1 can be explained by the decreased median bubble size compared to water (Fig. 5), which is due to the decreased surface tension. Indeed, smaller bubbles are more easily entrained by the liquid and are hence trapped inside large scale vortices more frequently. With increasing viscosity, the plume expansion decreases rapidly and the void fraction peak is located on the centreline of the column. Differences outside the plume (bubble rising zone) between the results from the shadowgraph technique and the optical probe are related to small bubbles trapped in vortices and moving downwards. Since the optical probe was pointing downwards, these bubbles could

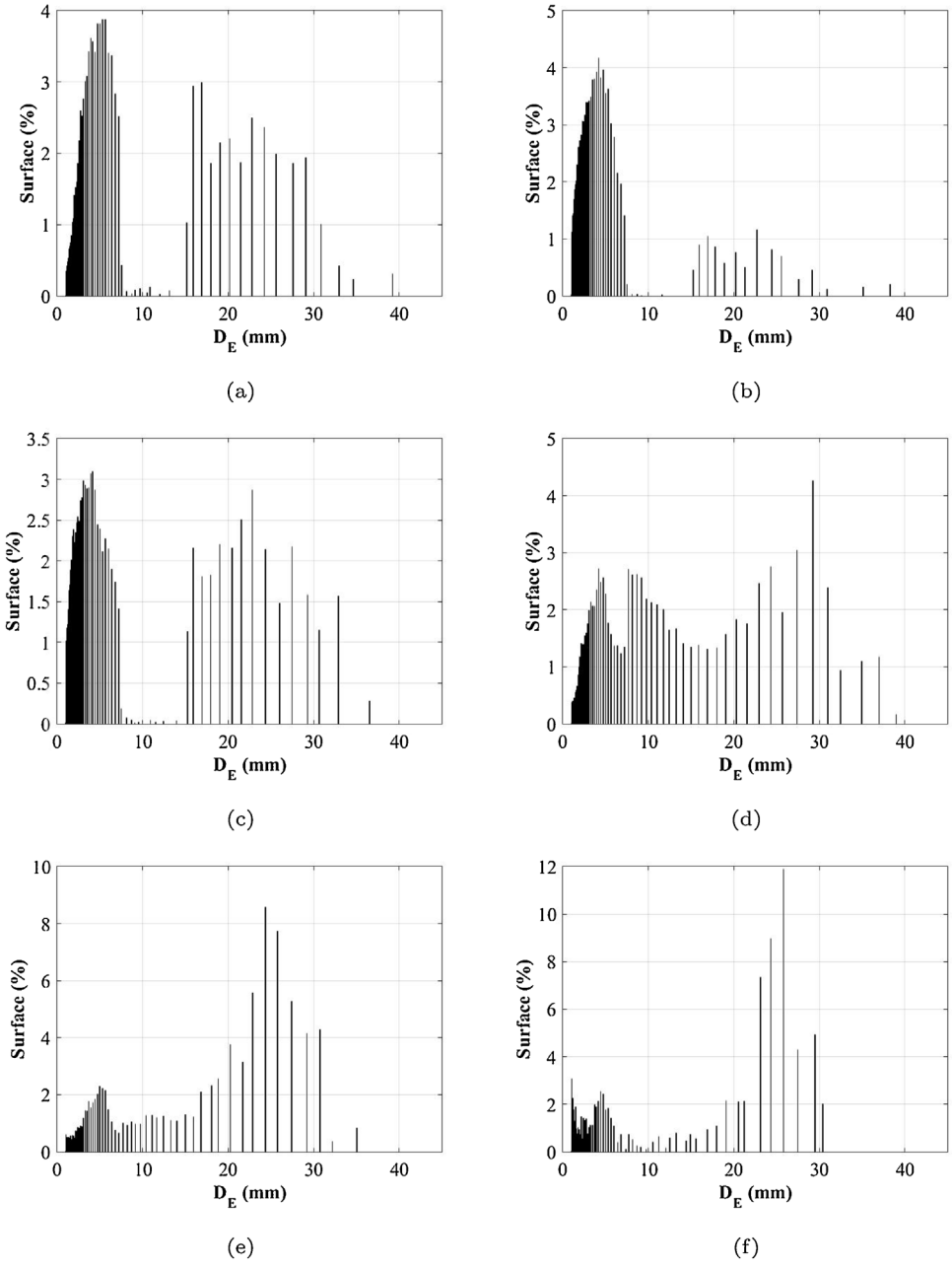

Fig. 7 – BSD with slugflow sparger in different fluids: a) water b) B1 c) B2 d) B3 e) B4 f) B5.

not be captured during measurements. Obviously, bubbles located inside the plume are exclusively rising. Thus, we can trust the results from the optical probe, especially in the inner half column ($X < 0.5$). The local void fraction profiles from Fig. 8d showed great reproducibility over three experiments. At the two highest viscosities considered here, only the void fraction value in the column centre was measured because the intrusivity of the probe broke the flow symmetry, rendering results erroneous. The averaged local void fractions were 1.1% in the case of fluid B4 and 3.1% in the case of fluid B5. As mentioned above, in the case of the slugflow sparger only the shadowgraph technique was applied for intrusivity reasons. However, Fig. 8b shows the normalized projected void fraction for CBs. Compared to the membrane sparger (Fig. 8a), the slugflow sparger generated bubble plumes that oscillated with less amplitude (Fig. 8b). All maximum peaks were located on or close to the centreline of the bubble column. The decreasing evolution of the plume width with increasing viscosity is similar to observations with the membrane sparger. In each fluid, the membrane sparger generated wider plumes than the slugflow sparger, independently of the viscosity. These results serve seamlessly for plume width estimations, complementing POPs.

3.4. *Gas velocity*

This section is dedicated to the gas phase velocity. Fig. 9 shows horizontal profiles of vertical and horizontal components of the mean gas velocity with corresponding RMS in the case of the membrane sparger. The vertcial dashed line indicates the maximum border cutting zone close to the centreline where the data treatment is likely to influence the results, mainly at high viscosities.

However, in the case of water, the magnitude of the mean vertical velocity is between 0.3 and 0.38 m/s over the whole plume width and exhibits a maximum peak close to its border at $X = 0.4$ (Fig. 9a). Outside the plume, the number of bubbles was not sufficient to achieve statistical convergence. At the

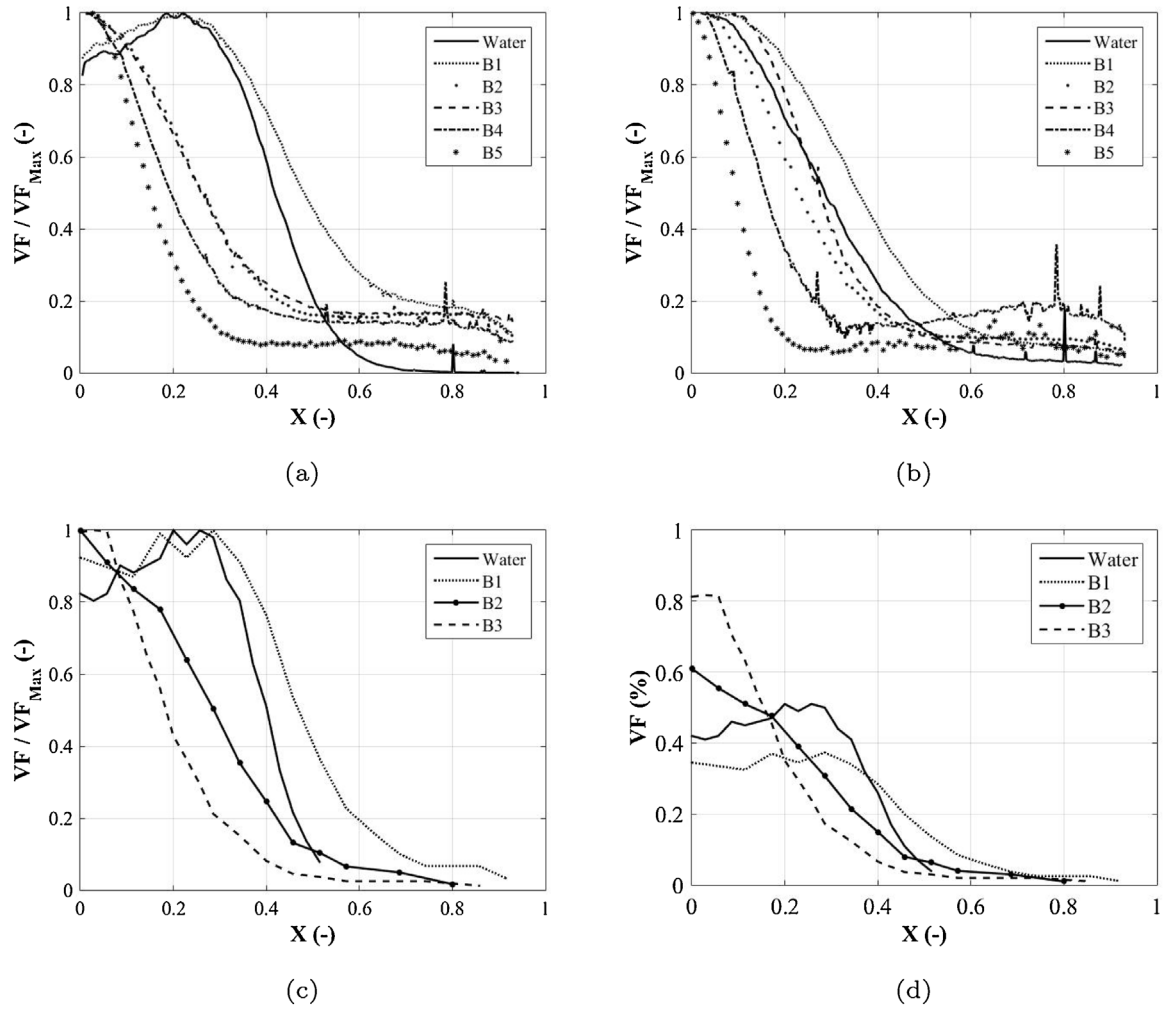

Fig. 8 – Time averaged void fraction profiles a) membrane sparger (EB) - normalized projected void fraction b) slugflow sparger (CB) - normalized projected void vraction c) membrane sparger (EB) - normalized local void fraction d) membrane sparger (EB) - dimensional local void fraction.

same viscosity, but with smaller bubbles than in water (fluid B1), the vertical mean velocity profile takes the same shape, presenting a peak at $X = 0.4$, with a slightly smaller magnitude. These gas velocities are close to the bubble terminal velocities of the size range considered (between 3 and 5 mm), indicating a weak liquid velocity, as expected for DCF. At higher viscosities, the maximum velocity is located on or close to the centreline of the plume and increases with increasing viscosity. Outside the plume, the vertical movement is more and more damped by the viscosity and approaches zero. Concerning the RMS of the vertical velocity component, a nearly flat profile with a magnitude between 0.075 and 0.1 m/s is observed in water (Fig. 9b). In the other fluids, the decreased surface tension generated enough small bubbles easily entrained by the liquid, to obtain statistical convergence over the whole column width. These small bubbles can be trapped inside large-scale liquid vortices, inducing large RMS values outside the plume as observed in the case of fluid B1, where the maximum peak is located around $X \approx 0.7$. With increasing viscosity, the maximum RMS peak shifts towards the centreline of the column and the RMS magnitude decreases close to the wall, where the velocity is around zero. As expected, the plume oscillations are damped by the viscosity. The mean horizontal velocity is plotted in Fig. 9c. The values indicate a weak horizontal movement towards the walls, which decreases with increasing viscosity. The magnitude of the corresponding RMS (Fig. 9c) is nearly one order of magnitude larger than horizontal mean values, unlike to the vertical RMS. The decreasing trend from the centreline towards the walls will be explained via time- and phase-averaged data of the liquid velocity (Section 4). With increasing viscosity, the amplitude of the horizontal oscillations decreases and tends to zero in fluid B5.

The same kind of information is plotted in Fig. 10 for the slugflow sparger. At low viscosity (water and fluid B1) a magnitude between 0.3 and 0.35 m/s is obtained over the whole plume. Differences between the two fluids are less pronounced than in the case of the membrane sparger since bubble sizes are close to each other (Fig. 7a and b). In addition, the rising velocity of large bubbles is less sensitive to interface contamination (Legendre et al., 2009). However, the increasing velocity on the centreline and the decreasing velocity close to the walls with increasing viscosity are similar to the profiles obtained with the membrane sparger. Further similarities were observed in the case of RMS profiles (Fig. 10b). As in the case of the membrane sparger, at low viscosity, the slugflow sparger generates a nearly flat profile over the plume width. Peaks observed previously at higher viscosities can not be identified in Fig. 10b. The magnitude of the vertical RMS in the inner region ($X < 0.3$) is always between 0.1 and 0.15 m/s whatever the fluid. In line with the membrane sparger, Fig. 10c also shows very weak horizontal mean velocities, close to zero. Compared to the horizontal mean velocity, the corresponding

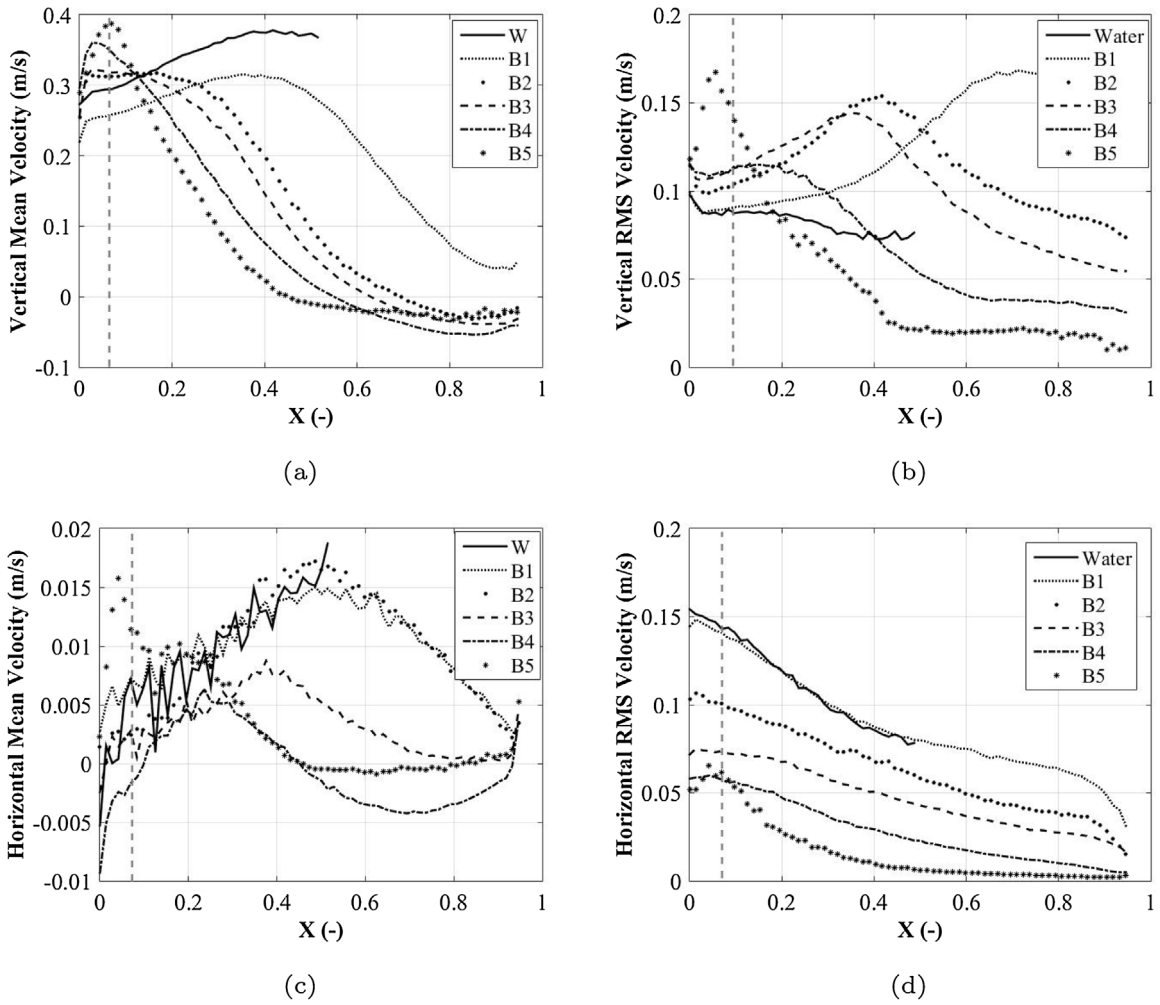

Fig. 9 – Time averaged gas velocity with membrane sparger (EB) in different fluids a) vertical mean velocity and b) corresponding RMS; c) horizontal mean velocity and d) corresponding RMS.

RMS (Fig. 10d) show large amplitudes. Like that of the membrane sparger, the magnitude is nearly one order larger than the mean values. The same decreasing trend from the centreline towards the walls was observed. Here again, the viscosity has a damping effect.

4. Results and discussion: liquid phase

After the gas phase, the liquid phase is now analysed in detail. As mentioned in Section 2, PIV measurements with an interrogation window, covering the right half of the column, were performed. Probability Density Functions (PDFs), time and phase averaged velocity profiles along the horizontal axis are presented to study the impact of viscosity on plume oscillations. However, as stated by Chatfield (1984), "*Anyone who tries to analyse a time series, without plotting it first, is asking for trouble.*" Thus, we choose to present raw data first.

4.1. *Instantaneous velocity*

Horizontal velocity signals versus time recorded in the column centre are plotted in Figs. 11 and 12 for the membrane and slugflow sparger, respectively. Clear oscillating behaviour is observed in the case of the first three fluids (water and fluids B1, B2) and with the membrane sparger. At intermediate viscosities (fluid B3 and B4), the signals become noisy, but oscillations can still be recognized. In case of the highest viscosity no oscillation can be observed.

Similar observations were made with the slugflow sparger (Fig. 12). The first three fluids (water and fluids B1, B2) show clear oscillating behaviour, but with slightly smaller amplitudes. fluid B3 is very noisy, but an oscillation frequency can be identified. In fluids B4 and B5 no period could be quantified.

The oscillating plume behaviour can also be illustrated by plotting PDFs of instantaneous velocities. Fig. 13 shows PDFs of the horizontal velocity recorded in the column centre ($X = 0.05$) for both spargers and all fluids. In water and fluid B1, both spargers show clear bimodal distributions, which are similar and in line with the sinusoidal signals of Figs. 11 and 12 . With increasing viscosity, velocities are damped and their distributions become narrow. The latter is composed of superposed bimodal and normal shaped distributions, which correspond to random motion. This indicates that no large-scale oscillations are observed in the case of the highest viscosity considered here (fluid B5).

4.2. *Time-averaged velocity*

In this section, long time measurements, averaged over a large integral number of POPs, are presented. Fig. 14 shows horizontal profiles of vertical and horizontal components of the mean velocity, corresponding RMS and the correlation $u_l'v_l'$ in the case of the membrane sparger. At low viscosity, the

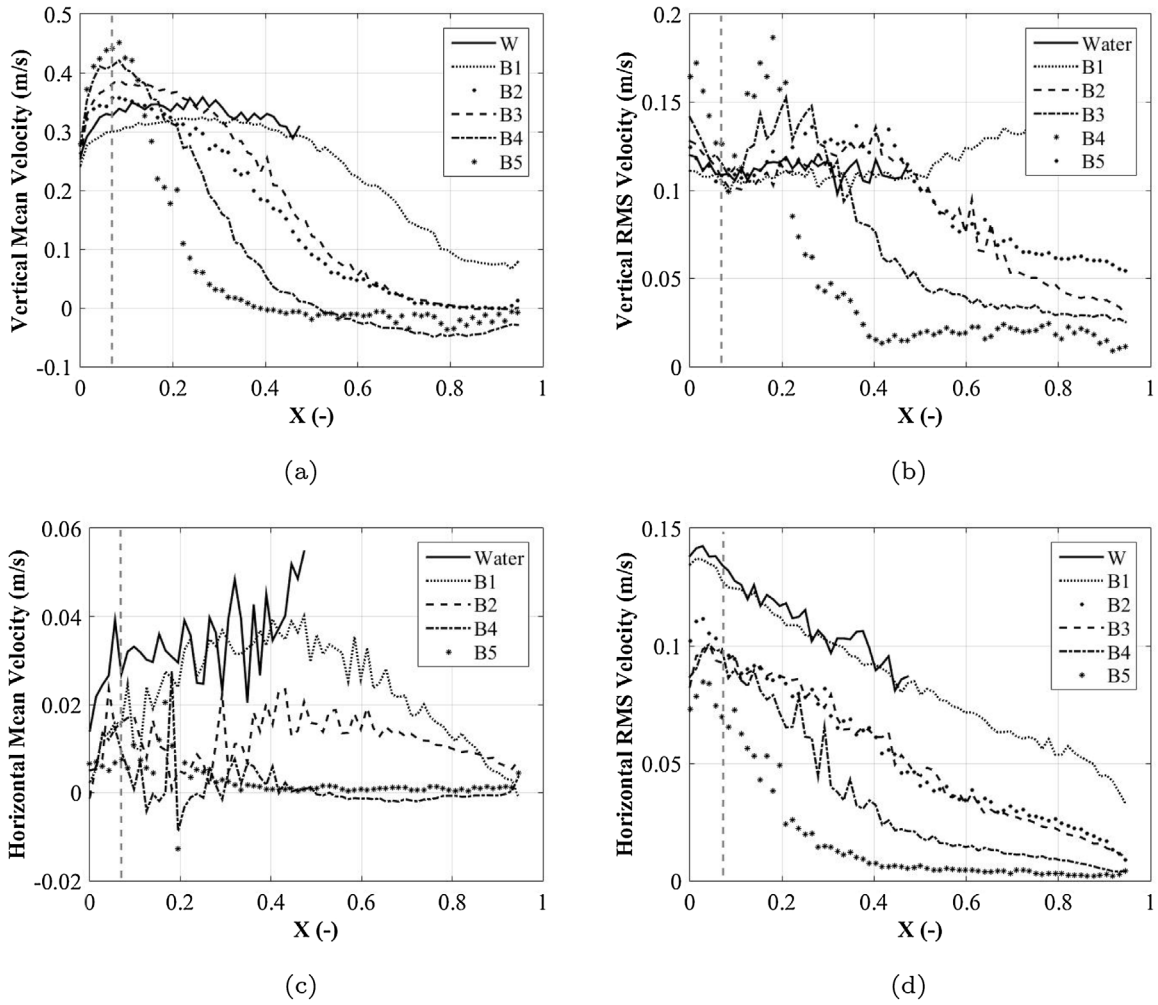

Fig. 10 – Time averaged gas velocity with slugflow sparger (CB) in different fluids at 50 *l*/*h* a) vertical mean and b) corresponding RMS velocity; c) horizontal mean and d) corresponding RMS velocity.

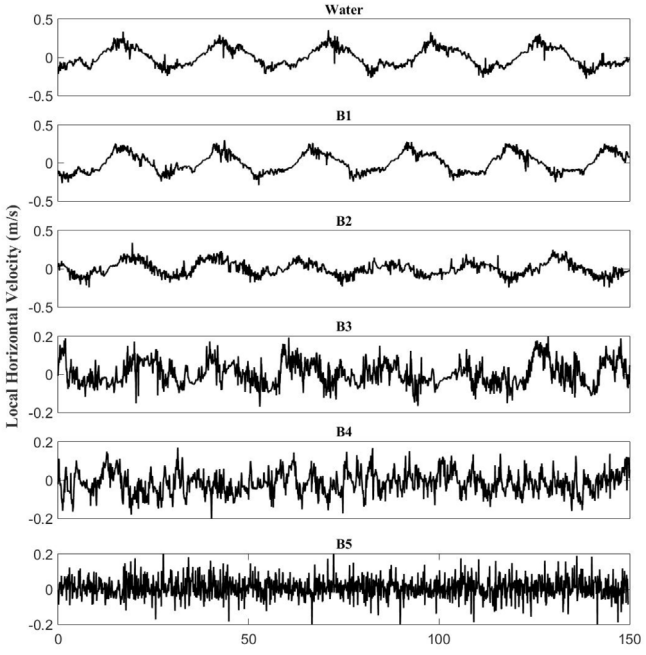

Fig. 11 – Horizontal velocity in the column centre (X = 0.05) in time with membrane sparger at 50 *l*/*h* in different fluids.

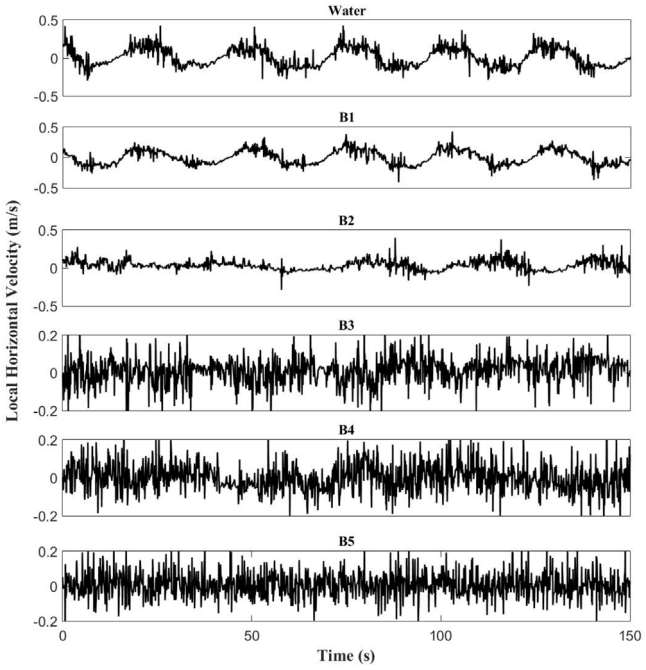

Fig. 12 – Horizontal velocity in the column centre (X = 0.05) in time with slugflow sparger at 50 *l*/*h* in different fluids.

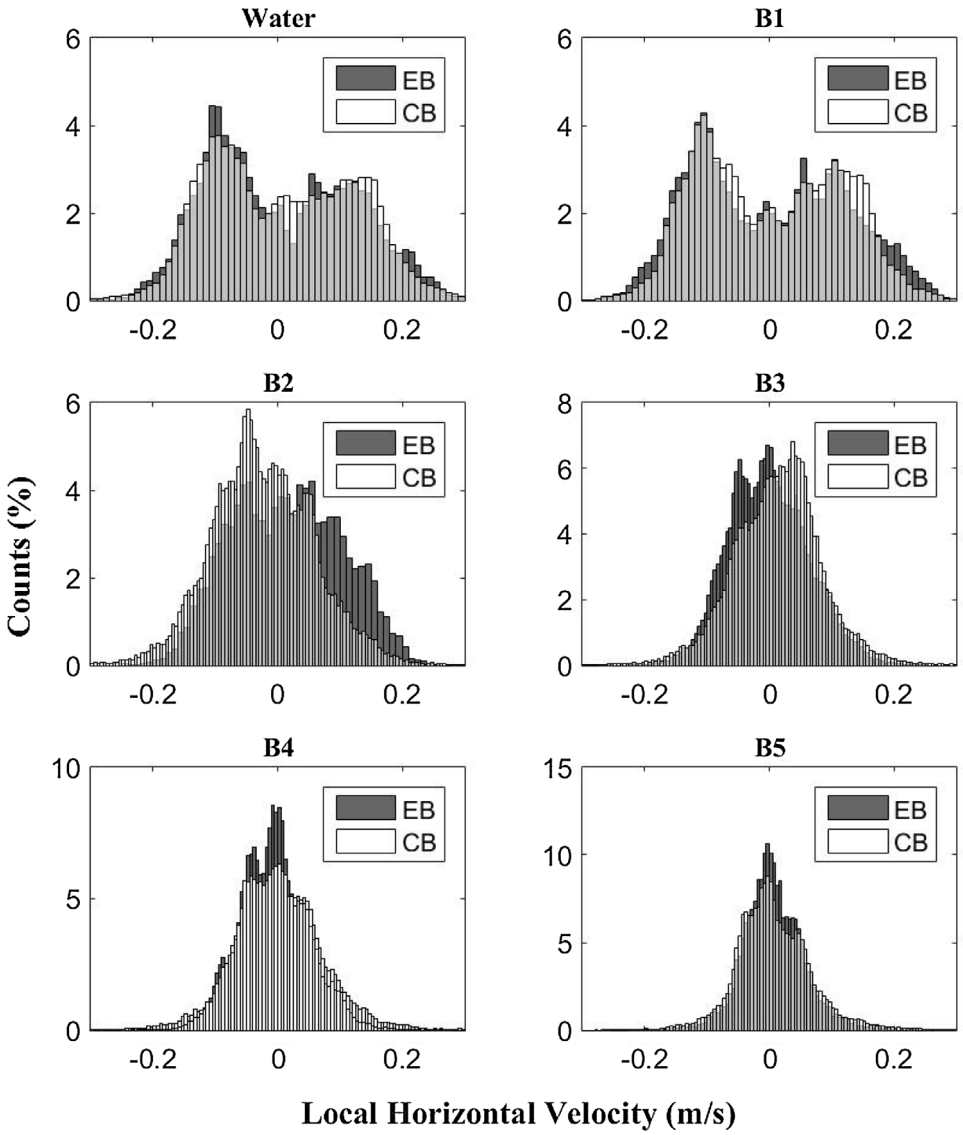

Fig. 13 – PDF of the horizontal velocity in the column centre ($X = 0.05$) with slugflow sparger at 50 l/h in different fluids.

vertical mean velocity (Fig. 14a) is very weak, between −0.05 and 0.05 m/s. With increasing viscosity the maximum velocity, located on the centreline of the column, increases to 0.3 m/s (DCF) and the recirculation zone becomes wider. The vertical RMS velocity (Fig. 14b) exhibits its maximum amplitude, which is three times larger than the mean flow at $X > 0.4$ in the case of water and fluid B1. As expected, the decreased surface tension has only a minor impact on liquid hydrodynamics. However, the RMS velocity on the centreline is close to 0.09 m/s and increases up to 0.12 m/s with increasing viscosity. The RMS velocity outside the plume decreases and rapidly approaches zero in case of fluid B5. The horizontal mean velocity, plotted in Fig. 14c, shows only small values for fluids with viscosities up to 20 $mPa.s$ (fluid B3), indicating weak horizontal movement. At higher viscosity, a very weak movement towards the column centre can be observed. The corresponding RMS (Fig. 14d) shows decreasing behaviour from the column centre towards the walls. Again, the surface tension has nearly no influence. However, the decreasing trend from the centre towards the wall can be analytically described by $\sqrt{\overline{u'^2}} \approx a\omega\sqrt{1-X^2}$ since on the centreline, $\sqrt{\overline{u'^2}}$ is proportional to $a\omega$. Its amplitude decreases with increasing viscosity and approaches zero outside the plume in the case of fluid B5. Figs. 14b, d and e present normal and shear fluctuating correlation tensors. Similar measurements were presented by Simiano et al. (2006) and Simiano et al. (2009). However, in this paper, such fluctuating velocity correlations will not be defined as Reynolds stress. $u_l'v_l'$ (Fig. 14e) presents a peak at a position X which decreases with increasing viscosity. The position of each peak is close to the inflection point of the mean liquid velocity ($d^2u/d^2x = 0$ or $du/dx = \max$). The axial RMS (Fig. 14b) are slightly larger than horizontal RMS (Fig. 14d). As will be demonstrated later, based on phase-averaged velocity profiles, RMS values can be explained by the periodic structure of the flow, induced by the oscillating bubble plume. This is not turbulence, but the trace of coherent structures (large liquid vortices flowing downward and in phase with bubble plume oscillations (Mudde et al., 1997).

Fig. 15 shows the same kind of information as Fig. 14, but in the case of the slugflow sparger. The general trends are close to the observations with the membrane sparger, suggesting a small impact of the BSD on liquid dynamics. The weak vertical mean velocity increases with increasing viscosity, while RMS amplitudes decrease. The horizontal mean velocity is, once again, weak and corresponding RMS profiles are similar to Fig. 14d. Results in Fig. 15e are close to the results of Fig. 14e.

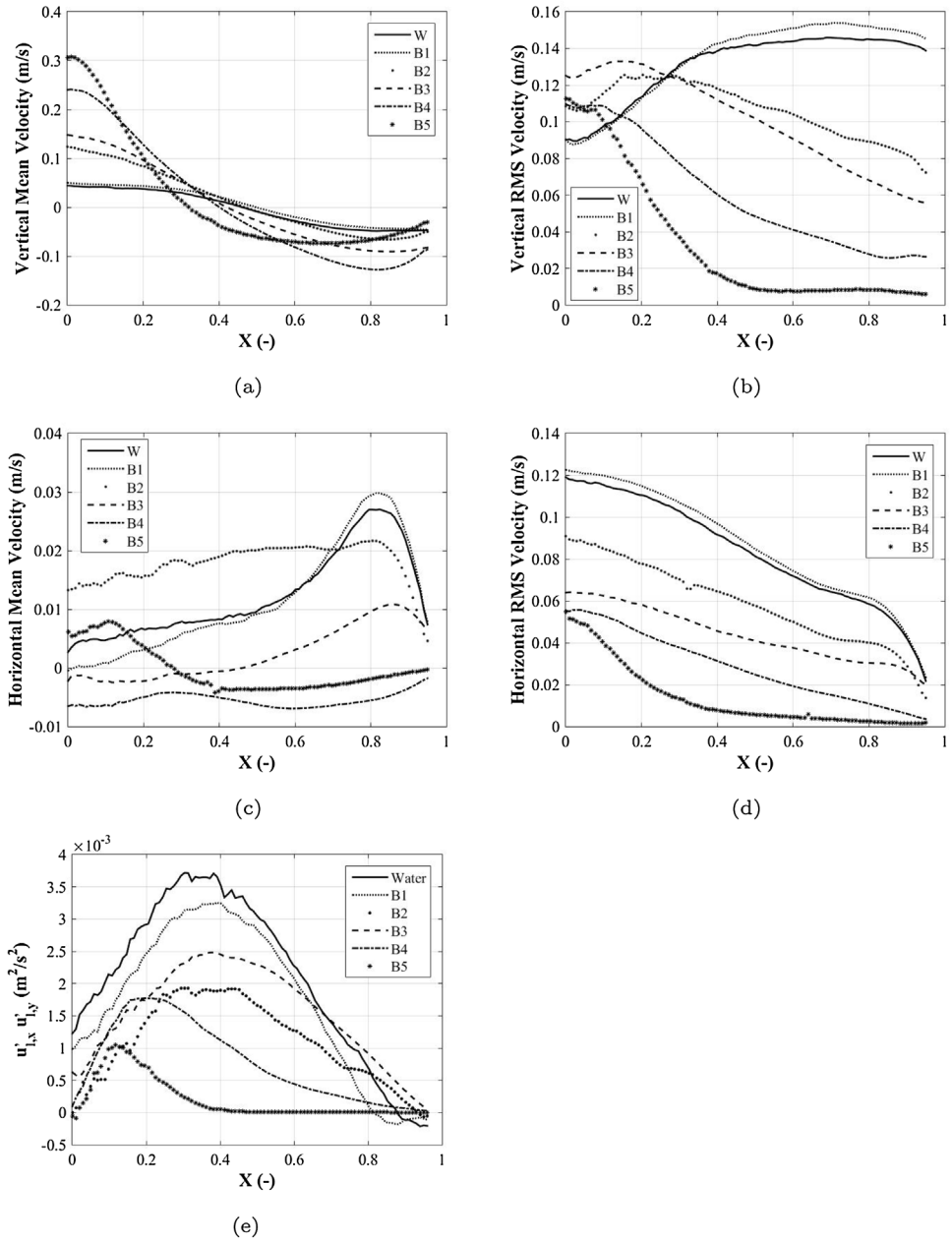

Fig. 14 – Time averaged liquid velocity with membrane sparger (EB) in different fluids at 50 l/h a) vertical mean and b) corresponding RMS velocity; c) horizontal mean and d) corresponding RMS velocity; e) $u_l'v_l'$.

4.3. *Phase-averaged velocity*

Considering PDFs (Fig. 13), it is clear that time averaging of data can lead to filtering and, thus, to loss of important flow information, which is why customized phase (or conditional) averaging was also applied to our measurements. The principle consists of identifying identical moments on each period. The corresponding instantaneous velocity profiles are averaged together to obtain a phase-averaged profile. Any time-dependent signal, illustrating the oscillating behaviour, can be used and the classical Hussain and Reynolds decomposition (Reynolds and Hussain, 1972) can be performed ($U = \overline{U} + \tilde{u} + u'$) where $\overline{U}$ stands for mean flow, $\tilde{u}$ for organised motion and u' for turbulence.

However, as demonstrated in Laupsien et al. (2021a), proper orthogonal decomposition (POD) is capable to seperate coherent structures like mean flow and organised motion from turbulence. Therefore, PIV measurements were decomposed into different modes with an orthogonal basis, depending on their energy. In this previous paper, it was shown that the two most energetic modes corresponded to the large-scale fluctuating motion induced by the bubble plume. These two modes can be combined to reconstruct the liquid velocity flow fields corresponding only to bubble plume oscillations:

$$\vec{V_k^{1,2}} = a_k^1\vec{\phi^1} + a_k^2\vec{\phi^2} \tag{3}$$

where $\vec{V_k^{1,2}}$ represents the k-th instantaneous velocity field, a_k^1 and a_k^2 the temporal scalars and $\vec{\phi^1}$ and $\vec{\phi^1}$ the time independent spatial modes of the first two modes. In this way, mean flow and turbulent fluctuations could be filterd. Two locations of the reconstructed flow field, point $X = 0.05$ for the horizontal velocity component and $X = 0.9$ for the vertical one, were chosen in order to follow bubble plume oscillations in time. The two velocity signals were filtered by a sliding average over 30 measurement points, corresponding to 2 seconds,

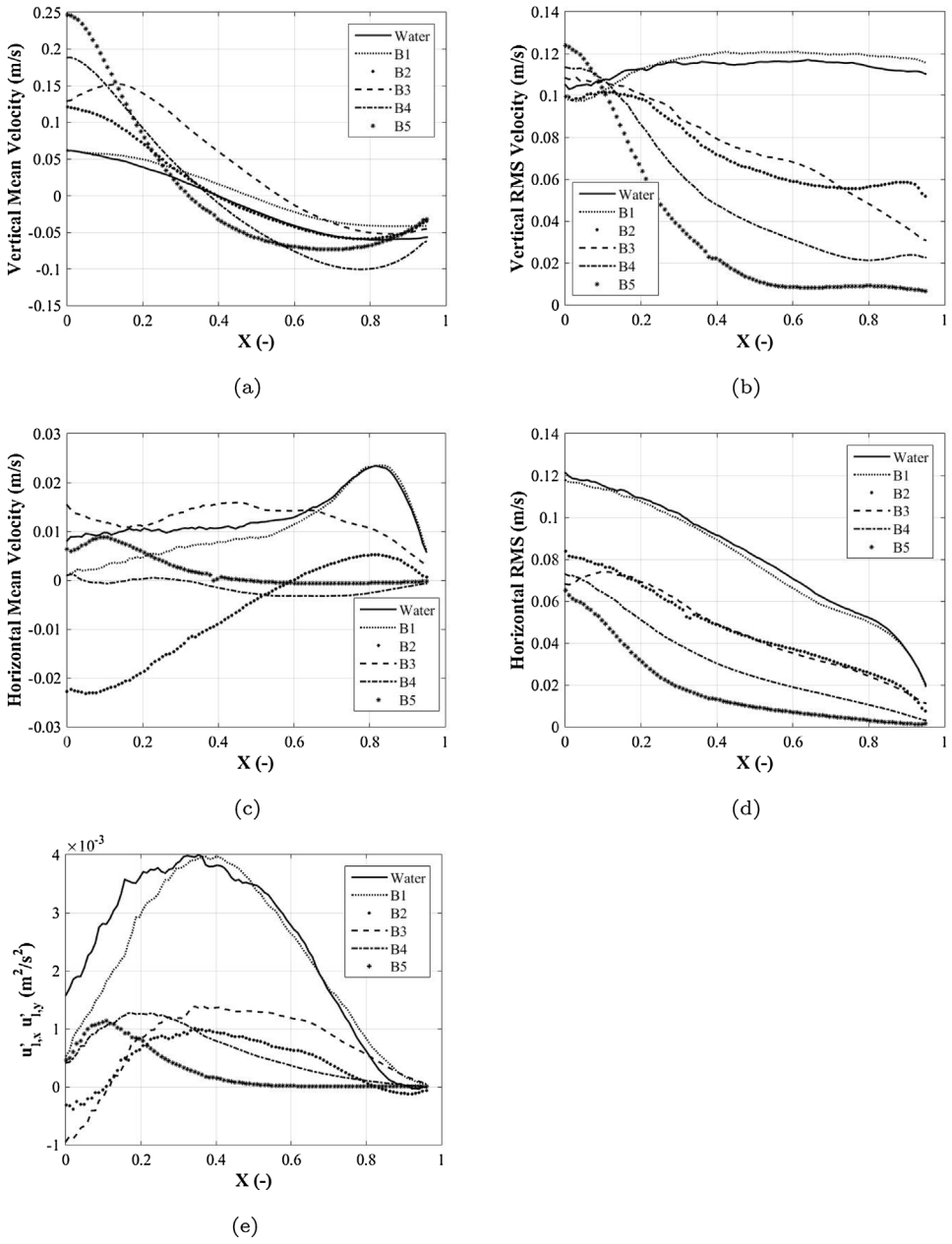

Fig. 15 – Time averaged liquid velocity with slugflow sparger (CB) in different fluids at 50 l/h a) vertical mean and b) corresponding RMS velocity; c) horizontal mean and d) corresponding RMS velocity; e) $u_l'v_l'$.

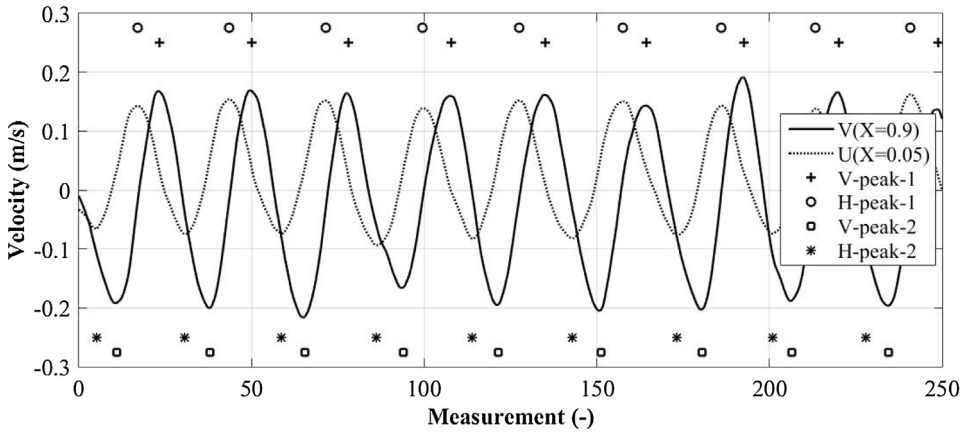

Fig. 16 – Water - EB - 50 l/h: identification of periodic moments on reconstructed velocity signals with the first two modes.

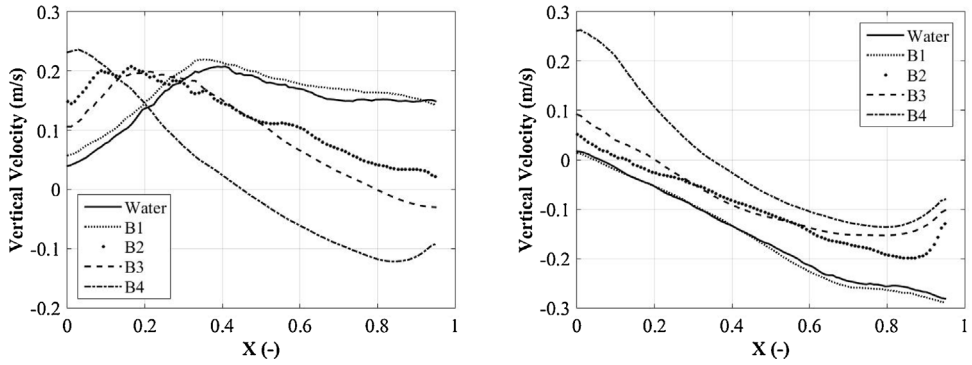

Fig. 17 – EB - phase averaged vertical liquid velocity profiles at a) t_0 and b) $t_0 + \frac{T}{2}$.

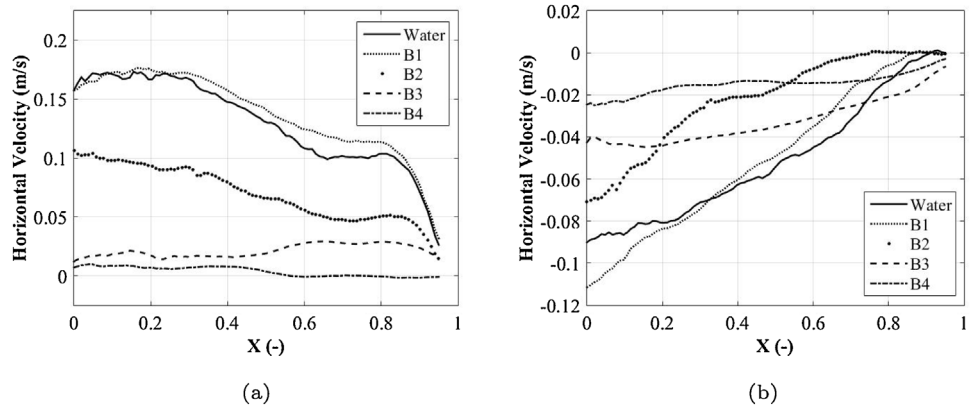

Fig. 18 – EB - phase averaged horizontal liquid velocity profiles at a) t_1 and b) $t_1 + \frac{T}{2}$.

to further improve phase (or conditional) averaged results. The two final velocity signals obtained for the membrane sparger in water are plotted in Fig. 16, where markers indicate the peak positions. Instantaneous horizontal velocity profiles, corresponding to each moment (for example to all circles), are reconstructed and then averaged together to obtain the final phase-averaged profile.

The peak positions corresponding to minima (□) and maxima (+) of the vertical velocity component (solid line) in Fig. 16 served to construct the phase averaged profiles in Figs. 17a (+) and b (□). Profiles from Fig. 17a (+) correspond to the instant t_0, when bubbles are mainly located inside the interrogation window (rising flow). At low viscosity (water and fluid B1), phase averaged velocity profiles show exclusively positive values and exhibit a maximum at the plume border, close to $X = 0.4$. As viscosity increases, the peak positions shift towards the centreline of the column. At the highest viscosity that still shows oscillating behaviour (fluid B4), the maximum velocity is nearly on the centreline and negative values indicate a recirculation zone.

Profiles from Fig. 17b (□) correspond to the moment $t_0 + \frac{T}{2}$, where bubbles are mainly located outside the interrogation window (descending flow). Profiles at low viscosity (water and fluid B1) show exclusively negative values and decrease linearly from the column centre towards the walls. With increasing viscosity, positive velocity values close to the centreline indicate a small zone with upward movement and a large recirculation zone. Fluid B4 shows comparable profiles at both moments, suggesting small oscillation amplitude. The flow structure changes towards DCF with constant rising movement in the inner column half and constant descending movement towards the walls as described by Diaz et al. (2006). Fig. 17 is very helpful for understanding Fig. 14b. It can be seen that, during one period, the vertical velocity of both water and fluid B1, varies between 0.2 m/s at t_0 ($X > 0.4$) and $-0.2\,m/s$ at $t = t_0 + T/2$. If we consider a sinusoidal trend with an amplitude of 0.2 m/s, the RMS is $0.2/\sqrt{(2)}$ (equal to $0.14\,m/s$), which corresponds to Fig. 14b.

Profiles from Figs. 18c (°) and 18 d (⋆) correspond to minima (°) and maxima (⋆) of the horizontal velocity (dotted line) in Fig. 16. Fig. 18c indicates a strong movement towards the wall at low viscosity. With increasing viscosity, the horizontal velocity component is more and more damped. In the case of fluid B4, nearly no lateral movement can be recognized. Fig. 18d shows a strong movement towards the centreline at low viscosity. Again, the viscosity increase damps the lateral velocity. At the highest viscosity, no lateral movement is present close to the wall ($X > 0.6$). This observation is in line with the quasi non-oscillating behaviour already mentioned during the discussion of the vertical component. It can further be concluded that the surface tension has nearly no impact on the liquid dynamics.

The same treatment was used in the case of the slugflow sparger, where the same periodic instants as with the membrane sparger were identified. Similarly to the case of the membrane sparger, Fig. 19 is helpful for analysing $u_{l,RMS}$ plotted in Fig. 14d. Both horizontal profiles of phase-averaged liquid velocity decrease with increasing X positon, explaining the decrease of $u_{l,RMS}$ plotted in Fig. 14d. At low viscosity, the curves of Fig. 19a exhibit a peak close to $X = 0.3$. Unlike the situation with the membrane, the peaks here remain at the same position with increasing viscosity, indicating a minor impact.

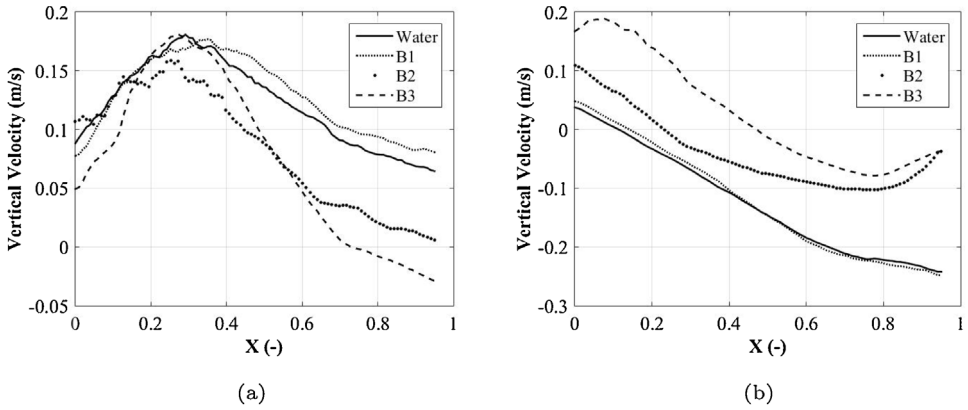

Fig. 19 – CB - phase averaged vertical liquid velocity profiles at a) t_0 and b) $t_0 + \frac{T}{2}$.

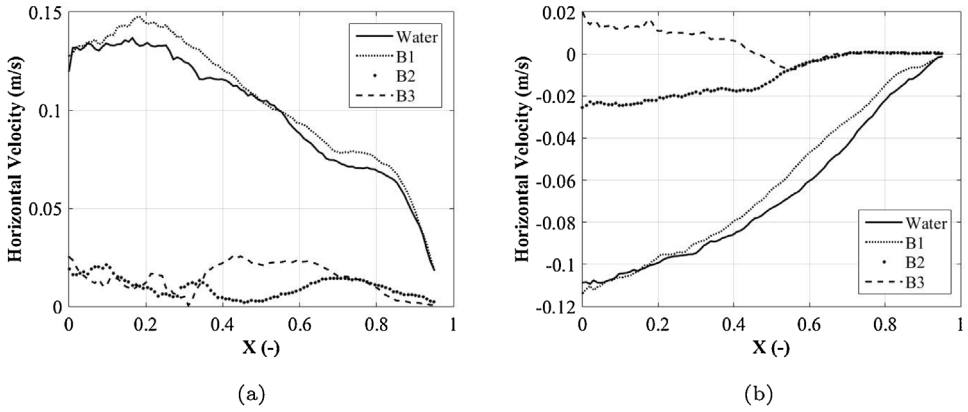

Fig. 20 – CB - phase averaged horizontal liquid velocity profiles at a) t_1 and b) $t_1 + \frac{T}{2}$.

Only the upward movement close to the wall decreases with viscosity increase. Fig. 19b shows an evolution similar to that made in Fig. 17b. The same descending movement over the whole interrogation window at low viscosity is observed. With increasing viscosity, positive values appear close to the centreline. Fluid B3 shows a rising zone of about the inner half column and a large recirculation zone towards the walls. The profiles of fluid B3 between the two instants considered confirm the weak oscillating behaviour mentioned above.

Observations in Figs. 20c and d are very close to the observations made in Figs. 18c and d. The lateral movement is slightly weaker than in the case of the membrane sparger, but the general trend with increasing viscosity is the same. The smaller velocity values compared to the membrane sparger confirm that the oscillating behaviour is less pronounced in the case of the slugflow sparger. The surface tension again shows only a minor impact on liquid dynamics.

Clearly, phase-averaged profiles reveal the periodic structure of the liquid flow, with coherent liquid velocities in phase with bubble plume oscillations. Consequently, bubble plume induced hydrodynamics are composed of a weak mean flow, energetic coherent structures and turbulence.

5. Conclusion

The influence of viscosity on bubble plume hydrodynamics have been investigated experimentally, using six Newtonian fluids with five different viscosities and two surface tensions. Two different spargers, a membrane and a slugflow tube, further broadened the experimental conditions. Shadowgraph images illustrate all flow conditions. Both phases were analysed in detail. Concerning the gas phase, the shadowgraph technique and an optical probe provided information about plume oscillation periods, bubble size distributions, plume expansions and gas velocities. The liquid phase was studied via PIV measurements. The data obtained were analysed via probability density functions, with time- and phase-averaging. The outcome when the membrane sparger was used indicated an impact of the viscosity on plume oscillation period and plume expansion whereas, with the slugflow sparger, only plume expansion was impacted and plume oscillation period remained constant. At the highest viscosity (100 $mPa.s$), no oscillation could be identified when gas was injected through the membrane. Concerning the slugflow sparger, at the second highest viscosity (50 $mPa.s$), oscillations could no longer be observed. The damping effect of the viscosity on plume oscillations could also be measured in the liquid phase. It must be mentioned that the two spargers generated different results concerning the gas phase but showed only a minor effect on liquid dynamics. The surface tension mainly impacted bubble size distributions, plume oscillation period and plume expansion, but showed hardly any effect on liquid hydrodynamics. It can be concluded that the main sensivity of plume hydrodynamics observed in this study is to viscosity. Bubble size distribution significantly influences the gas distribution, but affects the liquid flow only weakly. Probability density functions revealed organized motion that has been highlighted by phase averaging. In addition, the periodic flow contributes mainly to root mean square liquid and gas velocities.

Declaration of Interest

We wish to confirm that there are no known conflicts of interest associated with this publication and there has been no significant financial support for this work that could have influenced its outcome. No funding was received for this work.

References

Ali, Garmroodi Asil, Pour, A.N., Mirzaei, S., 2020. Intrinsic hydrodynamic investigation of three-phase bubble column: comparative experimental study on gas holdup. Theor. Found. Chem. Eng. 54 (2), 331–341.

Becker, S., De Bie, H., Sweeney, J., 1999. Dynamic flow behaviour in bubble columns. Chem. Eng. Sci. 54 (21), 4929–4935.

Becker, S., Sokolichin, A., Eigenberger, G., 1994. Gas-liquid flow in bubble columns and loop reactors: part II. comparison of detailed experiments and flow simulations. Chem. Eng. Sci. 49 (24, Part 2), 5747–5762.

Besagni, G., Inzoli, F., 2017. The effect of electrolyte concentration on counter-current gas-liquid bubble column fluid dynamics: Gas holdup, flow regime transition and bubble size distributions. Chem. Eng. Res. Design 118, 170–193.

Besagni, G., Inzoli, F., De Guido, G., Pellegrini, L.A., 2017. The dual effect of viscosity on bubble column hydrodynamics. Chem. Eng. Sci. 158, 509–538.

Buwa, V.V., Ranade, V.V., 2003. Mixing in bubble column reactors: role of unsteady flow structures. Can. J. Chem. Eng. 81 (3–4), 402–411.

Buwa, V.V., Ranade, V.V., 2004. Characterization of dynamics of gas-liquid flows in rectangular bubble columns. AIChE J. 50 (10), 2394–2407.

Cachaza, E.M., Elena Daz, M., Montes, F.J., Galan, M.A., 2011. Unified study of flow regimes and gas holdup in the presence of positive and negative surfactants in a non-uniformly aerated bubble column. Chem. Eng. Sci. 66 (18), 4047–4058.

Chatfield, C., 1984. The Analysis of Time Series: An Introduction, Sixth Edition. The Analysis of Time Series.

Chen, R.C., Reese, J., Fan, L.-S., 1994. Flow structure in a three-dimensional bubble column and three-phase fluidized bed. AIChE J. 40 (7), 1093–1104.

Delnoij, E., Kuipers, J.A.M., van Swaaij, W.P.M., 1997. Dynamic simulation of gas-liquid two-phase flow: effect of column aspect ratio on the flow structure. Chem. Eng. Sci. 52 (21–22), 3759–3772.

Delnoij, E., Kuipers, J.A.M., van Swaaij, W.P.M., Westerweel, J., 2000. Measurement of gas-liquid two-phase flow in bubble columns using ensemble correlation PIV. Chem. Eng. Sci. 55 (17), 3385–3395.

Devanathan, N., Dudukovic, M.P., Lapin, A., Lubbert, A., 1995. Chaotic flow in bubble column reactors. Chem. Eng. Sci. 50 (16), 2661–2667.

Diaz, M.E., Montes, F.J., Galan, M.A., 2006. Influence of aspect ratio and superficial gas velocity on the evolution of unsteady flow structures and flow transitions in a rectangular two-dimensional bubble column. Ind. Eng. Chem. Res. 45 (21), 7301–7312.

Etha, S.A., Jena, A., Lakkaraju, R., 2019. Clusterlike instabilities in bubble-plume-driven flows. Phys. Rev. E 99 (5), 053101.

Hikita, H., Asai, S., Tanigawa, K., Segawa, K., Kitao, M., 1980. Gas hold-up in bubble columns. Chem. Eng. J. 20 (1), 59–67.

Kazakis, N.A., Papadopoulos, I.D., Mouza, A.A., 2007. Bubble columns with fine pore sparger operating in the pseudo-homogeneous regime: Gas hold up prediction and a criterion for the transition to the heterogeneous regime. Chem. Eng. Sci. 62 (12), 3092–3103.

Kumar, S.B., Moslemian, D., Dudukovic, M.P., 1997. Gas-holdup measurements in bubble columns using computed tomography. AIChE J. 43 (6), 1414–1425.

Lapin, A., Lubbert, A., 1994. Numerical simulation of the dynamics of two-phase gas-liquid flows in bubble columns. Chem. Eng. Sci. 49 (21), 3661–3674.

Laupsien, D., 2017. Hydrodynamics, Mass Transfer and Mixing induced by Bubble Plumes in Viscous Fluids. Thesis. Toulouse, INSA.

Laupsien, D., Cockx, A., Line, A., 2017. Bubble plume oscillations in viscous fluids. Chem. Eng. Technol. 40 (8), 1484–1493.

Laupsien, D., Cockx, A., Line, A., 2021a. The organized flow structure of an oscillating bubble plume. AIChE J.

Laupsien, D., Le Men, C., Cockx, A., Line, A., 2019. Image processing for bubble morphology characteristics in diluted bubble swarms. Phys. Fluids 31 (5), 053306.

Laupsien, D., Le Men, C., Cockx, A., Line, A., 2021b. Labelled object velocimetry: simultaneous measurements of bubble size and velocity. Chem. Eng. Sci. 230, 116180.

Legendre, D., Sarrot, V., Guiraud, P., 2009. On the particle inertia-free collision with a partially contaminated spherical bubble. Int. J. Multiph. Flow 35 (2), 163–170.

Leon-Becerril, E., Line, A., 2001. Stability analysis of a bubble column. Chem. Eng. Sci. 56 (21), 6135–6141.

Lin, T.J., Reese, J., Hong, T., Fan, L.S., 1996. Quantitative analysis and computation of two-dimensional bubble columns. AIChE J. 42 (2), 301–318.

Liu, L., Yan, H., Ziegenhein, T., Hessenkemper, H., Li, Q., Lucas, D., 2019. A systematic experimental study and dimensionless analysis of bubble plume oscillations in rectangular bubble columns. Chem. Eng. J.

Lucas, D., Prasser, H.M., Manera, A., 2005. Influence of the lift force on the stability of a bubble column. Chem. Eng. Sci. 60 (13), 3609–3619.

Lucas, D., Ziegenhein, T., 2019. Influence of the bubble size distribution on the bubble column flow regime. Int. J. Multiph. Flow 120, 103092.

Mudde, R.F., Lee, D.J., Reese, J., Fan, L.-S., 1997. Role of coherent structures on reynolds stresses in a 2-D bubble column. AIChE J. 43 (4), 913–926.

Olivieri, G., Grillo, S., D'Errico, G., Marzocchella, A., Ruzicka, M., Salatino, P., 2013. Preliminary assessments of combined effects of surface tension and viscosity on bubble column hydrodynamics. In: Pierucci, S., Klemes, J.J. (Eds.), ICheaP-11: 11th International Conference on Chemical and Process Engineering, Pts 1-4, vol. 32. Aidic Servizi Srl, Milano, pp. 1579–1584.

Passos, A.D., Voulgaropoulos, V.P., Paras, S.V., Mouza, A.A., 2015. The effect of surfactant addition on the performance of a bubble column containing a non-Newtonian liquid. Chem. Eng. Res. Design 95, 93–104.

Pfleger, D., Gomes, S., Gilbert, N., Wagner, H.G., 1999. Hydrodynamic simulations of laboratory scale bubble columns fundamental studies of the Eulerian-Eulerian modelling approach. Chem. Eng. Sci. 54 (21), 5091–5099.

Rensen, J., Roig, V., 2001. Experimental study of the unsteady structure of a confined bubble plume. Int. J. Multiph. Flow 27 (8), 1431–1449.

Reynolds, W.C., Hussain, A.K.M.F., 1972. The mechanics of an organized wave in turbulent shear flow. Part 3. Theoretical models and comparisons with experiments. J. Fluid Mech. 54 (2), 263–288.

Ruzicka, M., Drahos, J., Mena, P., Teixeira, J., 2003. Effect of viscosity on homogeneous-heterogeneous flow regime transition in bubble columns. Chem. Eng. J. 96 (1–3), 15–22.

Ruzicka, M., Drahos, J., Thomas, N., 2001a. Effect of bubble column dimensions on flow regime transition. Chemie Ingenieur Technik 73 (6), 755.

Ruzicka, M.C., Vecer, M.M., Orvalho, S., Drahos, J., 2008. Effect of surfactant on homogeneous regime stability in bubble column. Chem. Eng. Sci. 63 (4), 951–967.

Ruzicka, M.C., Zahradni'k, J., Drahos, J., Thomas, N.H., 2001b. Homogeneous-heterogeneous regime transition in bubble columns. Chem. Eng. Sci. 56 (15), 4609–4626.

Simiano, M., Lakehal, D., Lance, M., Yadigaroglu, G., 2009. Turbulent transport mechanisms in oscillating bubble plumes. J. Fluid Mech. 633, 191–231.

Simiano, M., Zboray, R., de Cachard, F., Lakehal, D., Yadigaroglu, G., 2006. Comprehensive experimental investigation of the hydrodynamics of large-scale, 3D, oscillating bubble plumes. Int. J. Multiph. Flow 32 (10), 1160–1181.

Vial, C., Poncin, S., Wild, G., Midoux, N., 2001. A simple method for regime identification and flow characterisation in bubble columns and airlift reactors. Chem. Eng. Process. 40 (2), 135–151.

Wilkinson, P.M., Spek, A.P., Dierendonck, L.L.v., 1992. Design parameters estimation for scale-up of high-pressure bubble columns. AIChE J. 38 (4), 544–554.

Zahradnik, J., Fialova, M., Ruzicka, M., Drahos, J., Kastanek, F., Thomas, N.H., 1997. Duality of the gas-liquid flow regimes in bubble column reactors. Chem. Eng. Sci. 52 (21–22), 3811–3826.

Zahradnik, J., Kuncova, G., Fialova, M., 1999. The effect of surface active additives on bubble coalescence and gas holdup in viscous aerated batches. Chem. Eng. Sci. 54 (13–14), 2401–2408.